TABLE OF CONTENTS – CHAPTER 6.5 through 6.13

TABLE OF CONTENTS – CHAPTER 6.5 THROUGH 6.13 (CONT.)

TABLE OF CONTENTS – CHAPTER 6.5 THROUGH 6.13 (CONT.)

TABLE OF CONTENTS – CHAPTER 6.5 THROUGH 6.13 (CONT.)

6.5 Driver System Definition

Two driver designs have been developed for the IFE Reactor Design Studies program: a 4 MJ/pulse KrF Laser driver and a 7.8 MJ/pulse heavy ion driver. These IFE drivers (and their supporting subsystems) are described in this section.

A key element in the Prometheus reactor driver designs was to implement recent advances in high energy laser and heavy ion accelerator technologies. This enhanced performance, reduced risk, and promoted cost-effectiveness.

<u>Prometheus-L</u> – The MDA team selected an economical, reliable KrF laser amplifier design which is compatible with the non-linear optical (NLO) techniques pioneered during the past decade. The NLO techniques include:

(1) Use of stimulated rotational Raman scattering (SRRS) with large aperture beams, high energy beam synthesis, correction of dynamic optical beam distortions, and intensity smoothing to minimize UV optical damage.
(2) Replacing elaborate, multiple beam pulse compression systems with simple stimulated Brillouin scattering (SBS) pulse compressor driven by an electronically-controlled seed generator. This resulted in significant cost savings.

Implementation of NLO beam conditioning technologies has a profound effect on the Prometheus KrF laser driver design. These novel technologies permit the KrF excimer laser amplifiers to be optimized for performance and economy without having to meet simultaneously a very high output energy level (~200 kJ) or ambitious beam quality (BQ ~1) goal. The NLO technologies permit the Prometheus KrF laser driver to have superior operational characteristics at lower cost than conventional KrF laser designs.

<u>Prometheus-H</u> – A new look was taken at previous heavy ion driver design concepts together with some innovative techniques involved with superconducting magnets, auto-neutralization, self-focusing of heavy ion (HI) beams, etc. Key elements of the heavy ion driver include these innovative elements:

(1) A single LINAC operated in the burst mode to generate a series of HI pulses,
(2) Sequential pulses stored in appropriate storage rings,
(3) Triplet focusing magnets to collapse two sets of HI beams into compact beam bundles inside pre-ionized, self-pinched channels for transport to the target.

The success of this single accelerator/storage ring approach is heavily dependent upon improvements in Metglas to reduce core losses. Further cost reductions are possible by exploring a number of attractive attributes possessed by the Prometheus heavy ion driver design. These attributes may also help reduce costs of other plant elements. For example, the self-focused HI beam channel transport through the reactor target chamber shield, blanket, and wall to the indirect-drive DT target needs only two small entrance apertures. This improvement greatly simplifies the radiation shielding problems and inproves the first wall and blanket design and performance.

Prometheus drivers are designed to minimize the cost of electricity by employing redundancy where feasible in the key driver subsystems. These subsystems are designed in such a manner that the overall Prometheus driver requirements are met by using a multiple number of coordinated subsystems. The subsystems were optimized to maximize performance and cost-effectiveness, resulting in a more reliable and economical driver design.

The interrelationships of these Prometheus driver subsystems are described in detail in the subsequent sections.

6.5.1 Laser Driver Subsystems - The baseline Prometheus laser driver is composed of the following major subsystems:

(1) Excimer laser master oscillator (ELMO)
(2) Electric discharge excimer laser (EDEL) amplifiers (consisting of the excimer laser preamplifiers (ELPs), excimer laser drivers (ELDs), and excimer laser power amplifiers (ELPAs))
(3) Raman accumulators (together with their Stokes seed generators)
(4) SBS Pulse Compression Cells (together with their "chirper" seed generators)
(5) E/O Switchyard and Delay Lines
(6) Excimer Laser and NLO Cell Gas Flow Subsystems
(7) Beam Coupling Optics, Image Relaying, and Final Optics

A block-diagram of the Prometheus KrF laser driver architecture is provided in Figure 6.5.1-1. This figure also indicates the energy level, and beam pulse length, and number of components in each driver element.

As indicated in Figure 6.5.1-1, the 60 Prometheus KrF laser driver output beams are initiated with a single, carefully timed and synchronized 1 J pulse from the ELMO, followed by division of this initial ELMO beam into 1,020 beamlets by the beamsplitter array, followed by two tiers of ELPs (totaling 1,080 amplifiers) which amplify the beamlet energies up to 4 J, 1,020 ELDs which further increase the beamlet energies to 200 J, 60 ELD beams used to generate sixty 30 J Stokes seed beams, and the 960 ELPAs producing output energies of 6 kJ each. The 60 main beams are dominated by a NLO architecture—the Raman accumulator architecture is repeated 60 times. Arrays of 16 of the ELPA 6 kJ beams are injected into each of the sixty 120x120 cm aperture Raman accumulators prior to introduction into each of the 60 SBS pulse compressors. Following pulse compression and temporal tailoring, these 60 pulse-compressed beams are collimated and focused through the final focusing optics to generate the laser pulses which deliver 4 MJ of total energy on the direct-drive targets. A similar KrF laser driver system could be used for irradiation of indirect-drive targets.

The example illustrated in Figure 6.5.1-1 represents our preferred baseline design choice for the work-horse excimer laser chains; i.e., the case in which 960 moderate energy (~6 kJ), electric-discharge excimer laser (EDEL) amplifiers are used as the pump lasers for the 60 Raman accumulators. As noted above, also assumed in Figure 6.5.1-1 is the Prometheus laser driver configuration appropriate for illumination

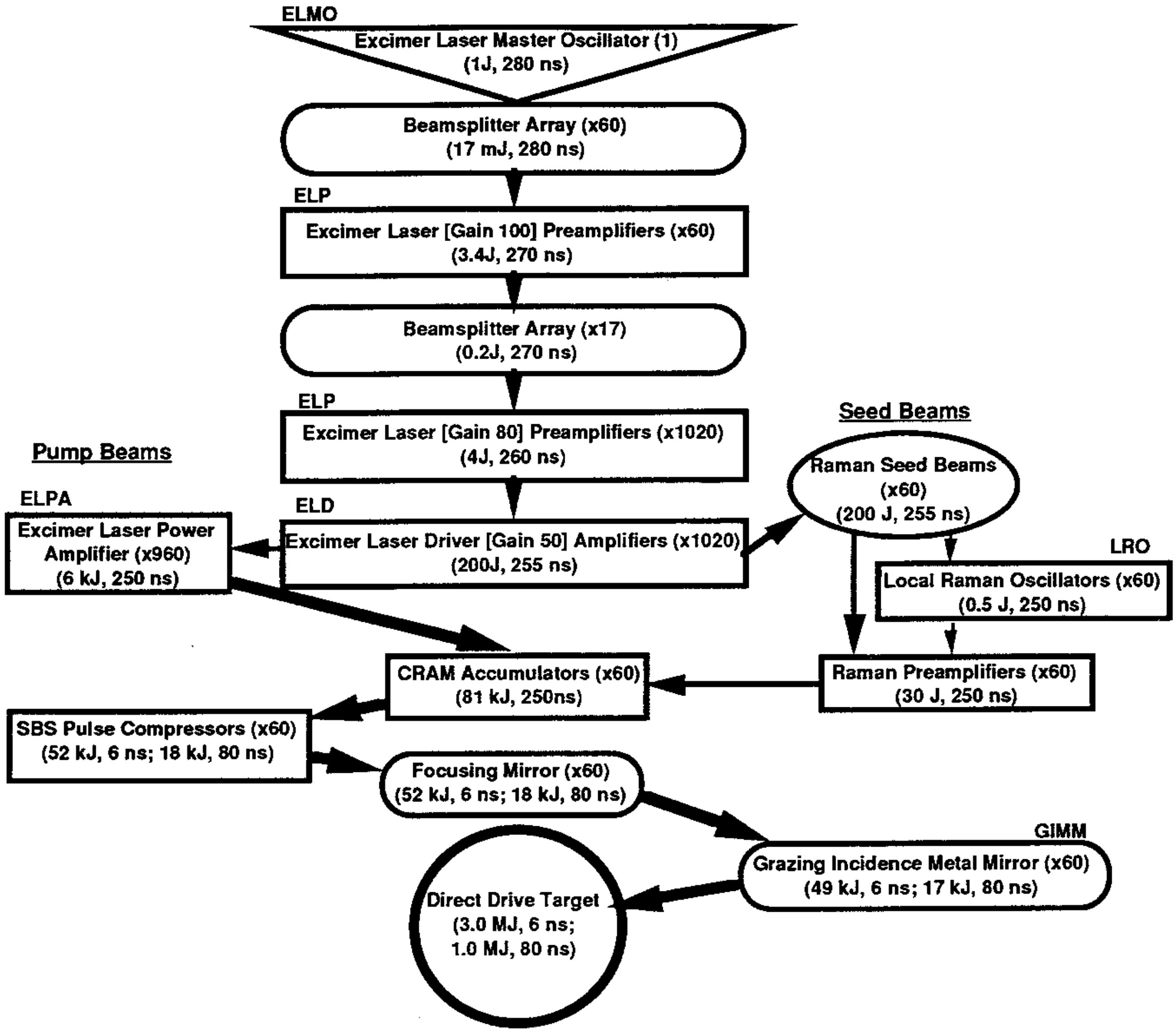

Figure 6.5.1-1 This block diagram illustrates how the PROMETHEUS ELMO pulses are beam-divided, amplified, accumulated, pulse-compressed, and focused onto the DT target.

of a direct-drive DT target (indirectly-driven laser targets require a different final focus laser beam configuration than shown). In order to illustrate the working relationships of these laser driver subsystems relative to each other, an overall simplified schematic of the Prometheus laser driver from the ELMO through the beamsplitter arrays, the ELPs, the ELDs, and the ELPAs to the Raman Accumulator is shown diagramatically in Figure 6.5.1-2.

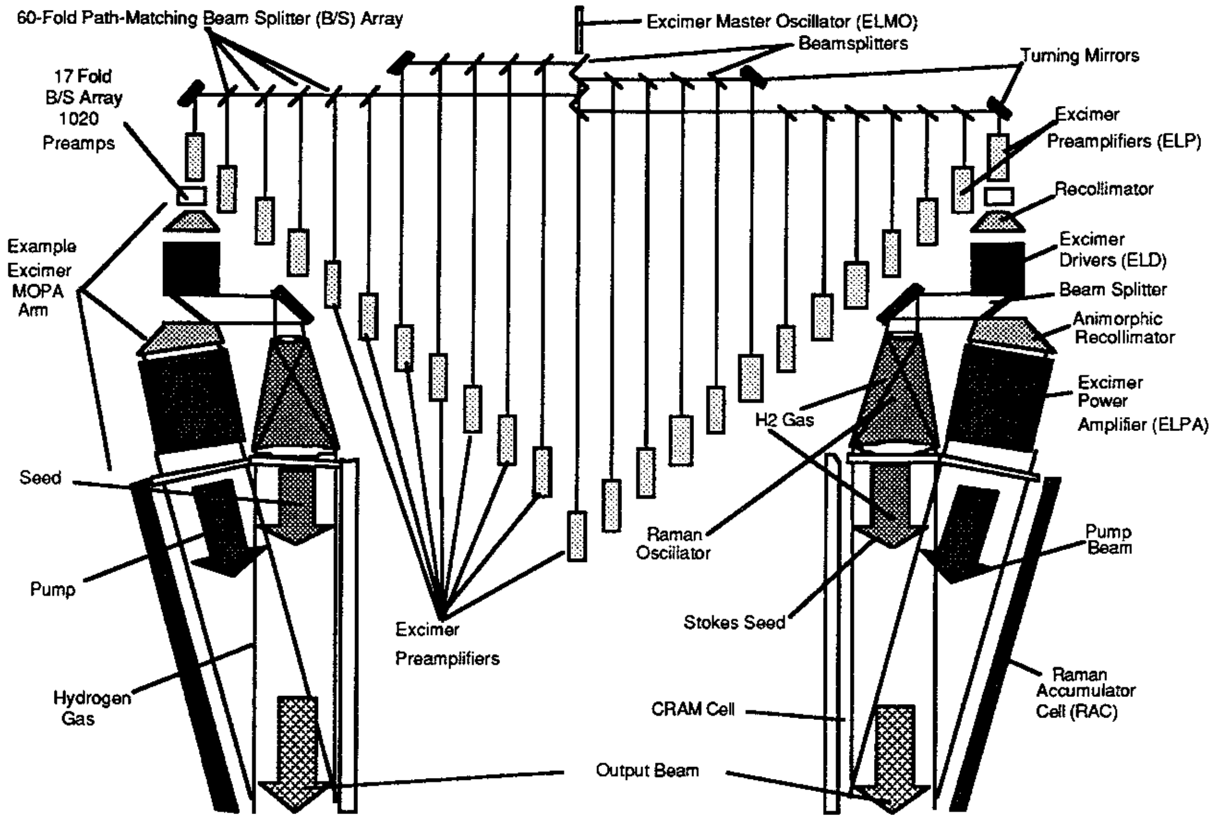

Figure 6.5.1-2 The 1 J output pulse from the ELMO is divided into 1020 beamlines, amplified by ELPs, ELDs, and ELPAs. The Stokes seeds are generated and injected into the Raman accumulators along with the main output beams.

In Figure 6.5.1-2, following division of the original single ELMO beam into 1,020 beamlets, the ELMO output pulse determines the phase, timing, intensity, etc., of the square output beams from the 1,020 ELPs, 1,020 ELDs, and 960 ELPAs. There are 60 additional excimer laser amplifier chains consisting of 60 ELPs and 60 ELDs. A small amount (0.5 J) of energy is split off from the 200 J output beams from each ELD and is fed into a Raman seed generator cell, path-matched with the original output beam from the ELD. This 100 mJ Stokes seed is then spatially filtered to improve beam quality, amplified in a Raman preamplifier having a gain of 300 up to a level of ~30 J, collimated to a 120-cm aperture, and injected into the 120x120-cm square aperture Raman accumulator. The 4x4=16 ELPA pump beams enter the Raman accumulator cell (RAC) at a slight angle, $\theta \sim 5^{o}$, to the RAC axis. In the baseline Prometheus excimer laser driver design, these 16 ELPA beams (each having an energy of ~6 kJ and a pulse duration of 250 ns (for EDEL ELPAs) or 500 ns (for EBEL ELPAs)) have square apertures of approximately 30x30 cm. These beams are combined (or "accumulated") in the large aperture (120 cm) Raman accumulator cells to yield an output beam of ~80 kJ. Note that electron-beam excimer laser (EBEL) amplifiers are an alternative technology which could be employed. This topic is discussed thoroughly in Section 6.5.1.2.2.

As discussed in Section 6.5.1.4, the beam qualities of the output beams from the ELPAs are not expected to be high, owing to the turbulent flow of gases through the excimer amplifiers, dynamic gas disturbances caused by excimer laser excitation, and other disturbing factors. However, the beam-crossed Raman (or CRAM) accumulator is able to improve the resultant beam quality of the excimer laser pumps considerably, so that the output beams from the Raman accumulators can be of excellent quality.

Following the Raman accumulators, each of the sixty ~80 kJ beams is then injected into each of the 60 SBS pulse compressors, as shown in the schematic diagram in Figure 6.5.1-3.

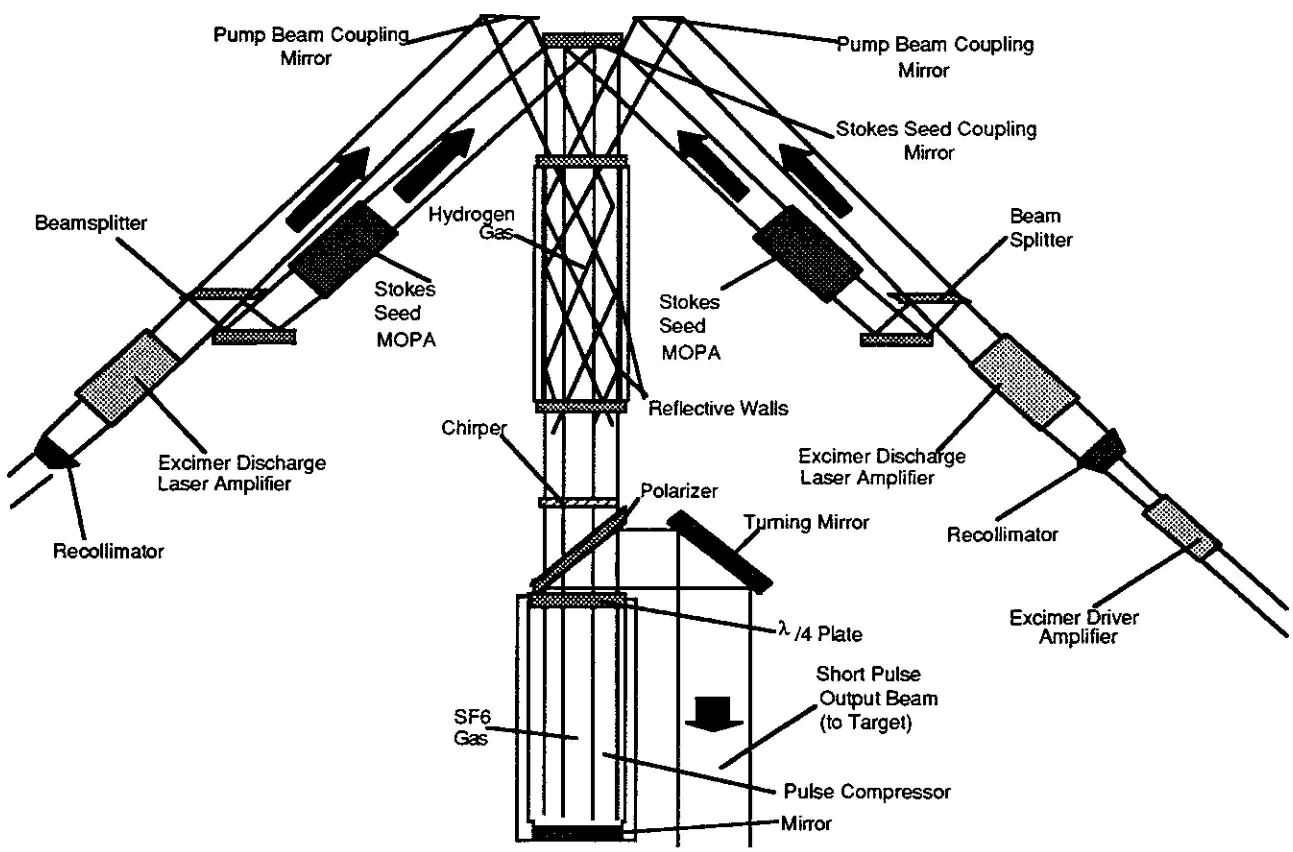

Figure 6.5.1-3 Following the conversion of the excimer pump beams in the Raman accumulators, the long 250-ns (for EDELs) or 500-ns (for EBELs) pulses are injected into the SBS pulse compressor cells where ~65% of the energy is converted into a 6-ns pulse using a ramped Stokes SBS seed.

As shown in Figure 6.5.1-3, the large diameter (~120 cm), high energy square output beams from the Raman accumulators are directed through a time-varying electro-optical modulator "chirper" which places a specific acoustical frequency shift on the leading 6-ns edge of the Raman accumulator pulse. This "chirper" element generates the Stokes seed for the stimulated Brillouin scattering (SBS) pulse compression cell.

The "chirper" is operated in a ramped mode to permit control over the compressed pulse shape (see Section 4.2.1 for a description of the variety of possible output pulse shapes obtained from SBS pulse compressor computer simulations).

Only approximately 70% of the laser energies in the 250 ns (EDEL) or 500 ns (EBEL) Raman accumulator pulses are converted into the short, 6 ns output pulses in the SBS pulse compressor. The remaining 30% of the beam energy remains in a long pulse duration (<250 or <500 ns respectively), is described as the "depleted SBS pump beam," and is available to supply the long, precursor pulse specified for the direct-drive DT target. Details of how this is accomplished can be found in Section 4.2.1. A precursor pulse has been defined as containing 35% of the total laser driver energy in the direct-drive target illumination requirements set forth by the Target Working Group.

Following pulse compression in the SBS cells, each of the 60 square laser beams is directed through an electro-optical switchyard for pulse tailoring, and then directed in 60 beams (assuming direct-drive) onto the DT target. A simplified, end to end diagram of the overall Prometheus laser driver system from master oscillator to DT target is provided in Figure 6.5.1-4.

The schematic diagram, Figure 6.5.1-4, illustrates the approximate optical arrangements of a single arm of the laser driver subsystems. For reasons of clarity, this figure does not illustrate the actual proposed Prometheus configuration of the laser driver subsystems that are described in Section 6.3.

The functions of each of these laser driver subsystems are briefly described in the following sections.

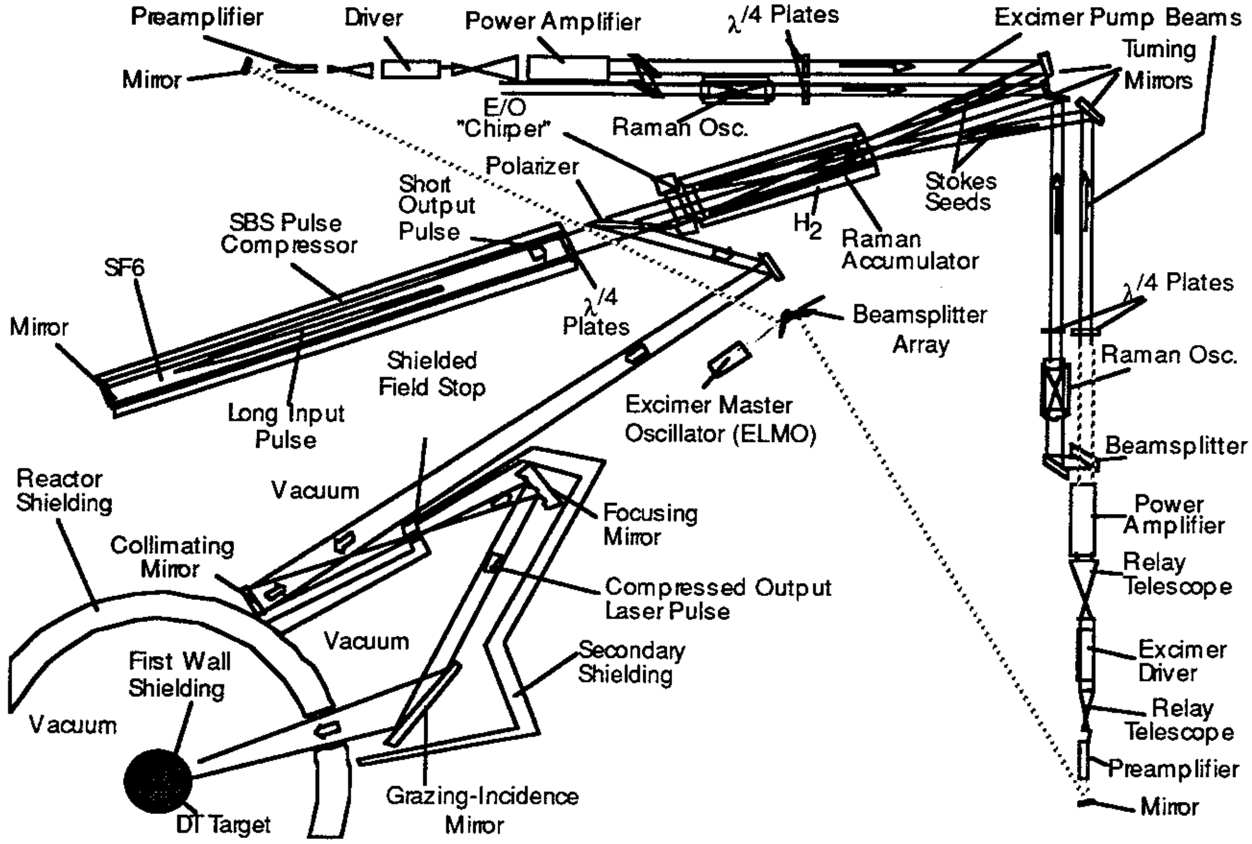

Figure 6.5.1-4 The output pulse of Prometheus laser driver is initiated at the ELMO, amplified by the EDELs, Raman converted in 60 Accumulator Cells, Pulse Compressed in 60 SBS Cells, and Focused onto the Direct-Drive Target with the Final Focus Mirror and the Grazing Incidence Mirror.

6.5.1.1 **<u>Excimer Laser Master Oscillator (ELMO)</u>** - As indicated in Figure 6.5.1-1, the generation of the Prometheus KrF laser driver's 4 to 6 MJ output pulse begins with the KrF excimer laser master oscillator (ELMO) emitting an initial pulse of ultraviolet (UV) laser light at λ = 248 nm (for KrF). The use of ArF at λ = 194 nm could also be used in this application. This pulse is first divided into 16x60 = 960 beam lines by a beamsplitter array, and then is successively amplified by KrF excimer laser preamplifiers (ELPs), excimer laser driver (ELDs), and excimer laser power amplifiers (ELPAs) to deliver output pulses of approximately 6 kJ each (960 beam lines). The output pulse from the ELMO needs to meet a series of requirements as summarized in Table 6.5.1-1.

The ELMO is the crucial timing and synchronizing element in the Prometheus laser driver. Although it can be triggered by signals derived from the DT target launching facility (see Section 6.4.4), the Prometheus laser driver computer control system monitors the output pulse shapes from the ELMO in multiple locations along the beam lines to assure that the input pulse shapes to the excimer laser amplifiers are appropriate for achieving the desired output pulse shapes and energies.

The ELMO characteristics are carefully selected to permit the excimer laser power amplifiers to be converted efficiently in the Raman accumulators and pulse-compressed in the SBS cells, thereby permitting the laser driver to generate the precise output pulse format required for DT implosion. In general, the spectral, temporal, and power characteristics of the ELMO output pulse will be changed in the process of efficient power extraction from the excimer laser power amplifiers (ELPAs), and thus the ELMO pulse characteristics must be deconvolved in order to produce the desired results at the ELPA output apertures.

Since the laser pulses originate with the ELMO, it is crucial that this subsystem be at least doubly redundant in order to prevent failure of the ELMO from forcing a shutdown of the reactor. Thus, it is recommended that three ELMOs be on line at the same time with one unit active, one unit on standby, and one unit capable of being activated in a matter of seconds.

The general specifications for the ELMO are summarized in Table 6.5.1-1.

Table 6.5.1-1 Prometheus ELMO Specifications

Parameter	Nominal Value	Unit of Measure
Number of Units	3 (for redundancy)	
Wavelength	248	nm
EDEL Mode Pulse Duration	280 (650, EBEL)	ns
Output Energy	1	J
Bandwidth	5	GHz
Polarization State	Linear	
Aperture	1x1	cm
Gain Length	100	cm
Output Fluence	1	J/cm^2
EDEL Mode Output Intensity	3.8 (1.5, EBEL)	MW/cm^2
Repetition Rate	5	Hz
Mean Firings Between Failures	10^{10}	
Number of 50% R Beamsplitters	490	
Number of Output Beamlines	1020	
Number of Diagnostic Beamlines	10	

The specific parameter values listed in Table 6.5.1-1 represent nominal values appropriate for high performance from the Raman and SBS cells. Thus, for example, the bandwidth of the ELMO output pulse can be varied over a wide range, from a minimum of a few GHz to a maximum of more than 1000 GHz (10^{12} Hz). Similar adjustments can be made in the other parameters to support different excimer laser driver design points.

6.5.1.1.1 ELMO Excitation Design - The ELMO excitation design is similar to that described below for the ELP, ELD, and ELPA units. Depending upon the excimer laser technology, iEDELs or EBELs, each amplifiers will conform to one of these two general categories.

6.5.1.1.2 ELMO Performance Characteristics - The ELMO is designed to be a versatile laser pulse generator with wide bandwidth ranges, output energy, and polarization state. Pulse durations are typically selected for the type of excimer laser chain (EDEL or EBEL) and are corrected for amplifier saturation in the excimer amplifiers, shortening the output pulse durations.

6.5.1.2 Excimer Laser Amplifiers - There are three general types of excimer laser amplifiers proposed for use in the Prometheus KrF laser driver. These are the excimer laser preamplifiers (ELPs), the excimer laser drivers (ELDs), and the excimer laser power amplifiers (ELPAs). In addition to these excimer laser amplifier types, there are also two possible choices of excimer laser excitation: electron beam excimer lasers (EBELs) and electric discharge excimer lasers (EDELs). These two types of excimer laser amplifiers will be described and each of these different excimer laser amplifier sizes will be briefly described below.

6.5.1.2.1 Electric Discharge Excimer Laser (EDEL) Amplifiers - The EDEL amplifiers are a class of amplifier for which the principal excitation technique of the excimer gas is a preionized electric discharge. In this geometry, an ionization mechanism (such as ultraviolet light, an electron beam, etc.) produces a sufficient ion density in the active medium to permit an efficient volumetric discharge to excite the upper laser level of the KrF (or ArF) excimer molecule. The primary source of excitation energy in this geometry is provided by the electric discharge (and its external pulsed power circuit).

A schematic cross-sectional diagram of an EDEL prototype amplifier excitation geometry is shown in Figure 6.5.1-5.

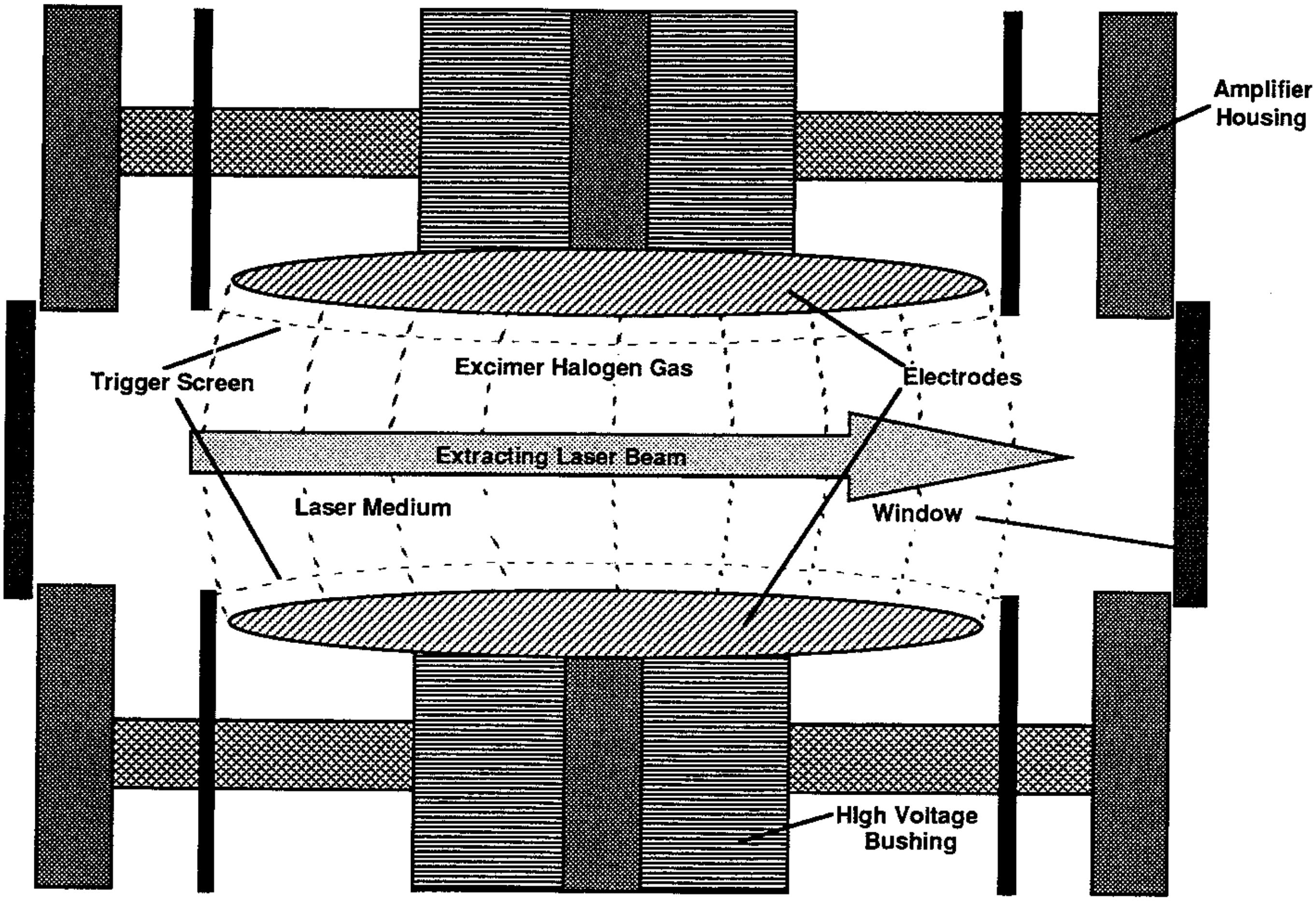

Figure 6.5.1-5 The electric discharge excimer laser (EDEL) excitation geometry provides for direct excitation of the KrF excimer via electric discharges between electrodes immersed in preionized volumes.

Note that the output apertures of these EDEL amplifiers are typically rectangular or square because the excitation geometry is rectangular. Theoretical studies[1,2] of the EDEL have suggested that increased laser amplifier pumping efficiencies could be achieved with direct electric discharge excitation of the excimer fuel. This increased efficiency appears promising for the following reasons:

(1) Excitation of the excimer gas occurs by direct contact with the electric discharge between the electrodes with no electron energy losses in a vacuum barrier (foil, Hibachi, etc.).

(2) Excimer laser excitation in an EDEL is expected to occur along the neutral channel[2] with the discharge optimized to populate the upper laser level of the 248 nm transition, thereby reducing the number of excited states generated in the active medium to only those leading to the appropriate inversion density.

(3) Reduced heating of the laser gas by the discharge current should occur with excitation along the neutral channel, thereby reducing gas dynamic-induced deterioration of amplifier beam quality.

There are a number of disadvantages associated with direct electric discharge excitation. These include:

(1) Only relatively small cross-sectional diameters (<35 cm) are feasible with electric discharge excitation, thereby limiting the output energies of the laser amplifiers to values of approximately 6 kJ. Optimized EDELs may produce even less energy.
(2) Instabilities arise in the electric discharge owing to temporal impedance changes caused by consumption of fluorine,[2] thereby limiting the pulse duration of the laser and increasing the cost of the pulsed power.

It is important to recognize, however, that the preceding discussion of EDELs is primarily based upon initial theoretical work, and both additional analysis and significant experimental EDEL development is essential if the relative promise of a KrF (or ArF) EDEL is to be properly assessed.

6.5.1.2.2 <u>**Electron-Beam Excited Excimer Lasers (EBEL)**</u> - Although the baseline Prometheus-L KrF laser driver design does not include the use of e-beam excited excimer lasers, considerable research and development has been carried out on these devices[3,4,5,6] and their inclusion in a future ICF laser driver design may occur if some of the more pressing technological problems with the amplifiers can be solved.

In the case of e-beam excited excimer lasers (EBELs), the entire excitation energy of the amplifier volume is delivered by relatively high energy electrons (<1.5 MeV), delivered at relatively high currents (~1 MA), transmitted through a foil barrier between the excimer fuel and the high vacuum of the electron beam machines.[5,6,7] This geometry is very useful for exciting relatively large volumes of gas (cubic meters) with large amplifier apertures (~1 m). Like the EDEL excitation geometry described above, the output apertures of EBELs tend to be rectangular or square.

Electrons having energies >0.6 MeV can produce serious radiation effects, such as the generation of γ-rays, photo-disintegration of nuclei, formation of color centers in transmissive optics (such as EBEL amplifier windows), etc. In addition, the energetic e-beams may excite excimer and other atomic energy levels which do not lead to the generation of an inversion density at the desired upper laser level of KrF (or ArF). A cross-sectional diagram of an EBEL prototype amplifier excitation geometry is shown in Figure 6.5.1-6.

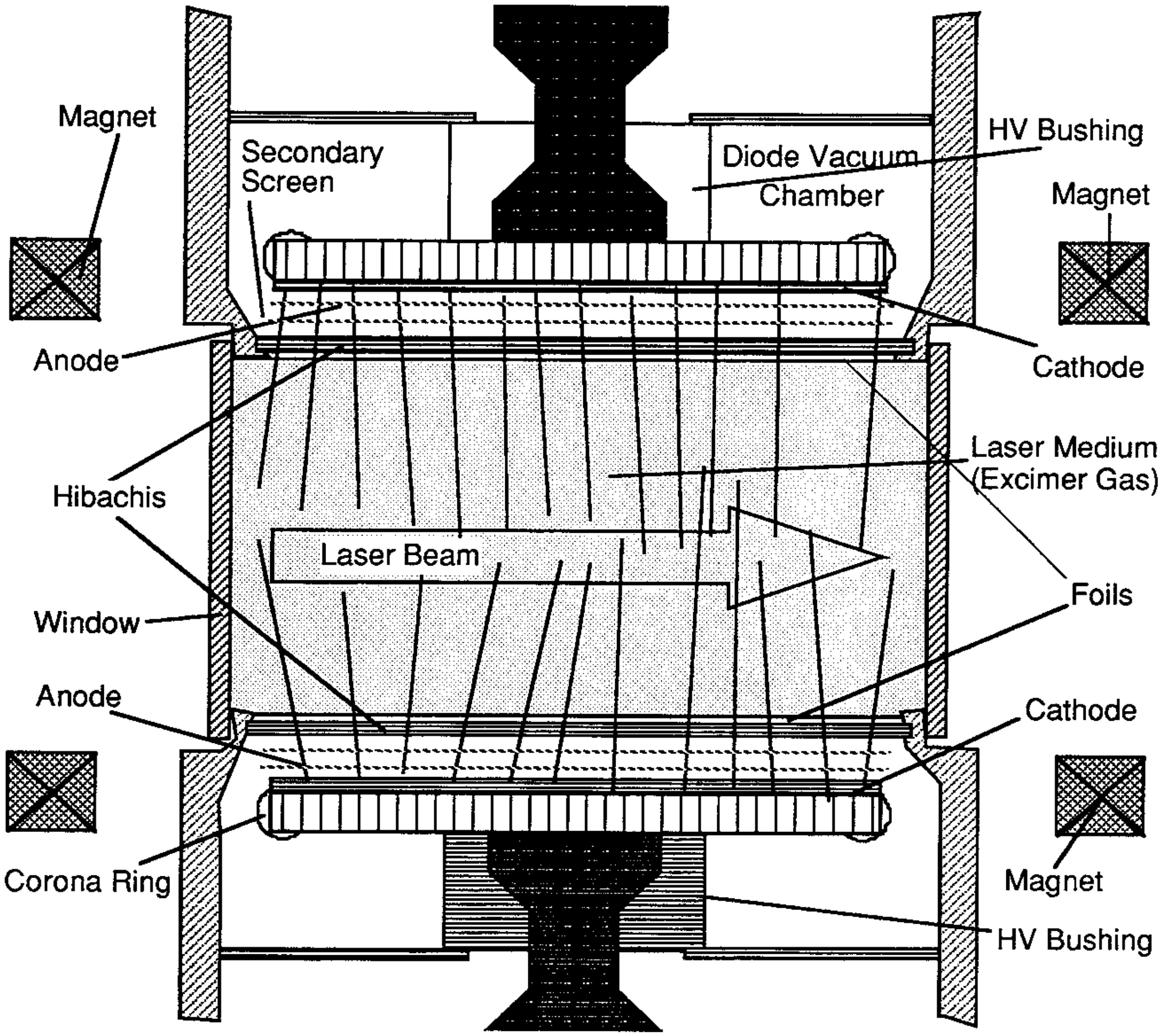

Figure 6.5.1-6 The electron-beam excited excimer laser (EBEL) excitation geometry permits larger volumetric excitation of the KrF excimer via direct e-beam excitation transmitted through a Hibachi and foil vacuum barrier.

As shown in Figure 6.5.1-6, the high energy (~1 MeV), high current (~1 MA) electron beams are generated in a high vacuum diode adjacent to a thin foil supported on a mechanical structure referred to as a Hibachi. These high energy, high current beams must then be transmitted through the thin foils (assuming double-sided illumination, as illustrated) and Hibachi structures where they subsequently interact with the Kr, F_2, Ar, etc., gases located at approximately a total pressure of 1 atm (760 torr). Under these conditions, a large number of excited states are created in the newly formed KrF excimer molecules. Some of these excited states lead to the formation of an inversion density for the desired λ_{laser} = 248 nm (or λ_{laser} = 194 nm) transition(s). Excitation of other energy levels in the excimer fuel ends up as heat which may cause laser beam quality problems.

Advantages associated with e-beam excitation of excimer laser amplifiers are:

(1) Large apertures (D ~ 1 m) and large volumes (V ~ 2 m^3) can be excited with relatively high uniformity.
(2) Relatively long pulses can be used (τ ~ 600 ns) to excite the excimer gas, thereby relaxing pulsed power requirements.
(3) A relatively large number of experiments have been carried out demonstrating the efficiency of the excitation technique.

Some disadvantages to the EBEL are:

(1) Transmission of high voltage, high current electron beams through thin foil/Hibachi structures has proven to cause reliability problems.
(2) If foil rupture occurs, the vacuum diode is flooded with hot, fluorine-containing fuel from the gain volume of the laser amplifier. As a consequence, damage can occur to the cathode, high voltage bushing, etc., increasing repair cost and time.
(3) Although the EBEL can theoretically be constructed at large apertures and volumes (Advantage #1), amplified spontaneous emission (ASE) and parasitic oscillations can occur in these larger excimer amplifier volumes, thereby reducing efficiency.
(4) Since the e-beams are transmitted through foil/Hibachi structures and excite numerous energy levels which do not result in achievement of the specific inversion density appropriate for the desired laser transitions (λ_{laser} = 248 nm [or λ_{laser} = 194 nm]), reduced pumping efficiencies and lowered beam qualities can be expected.

The Prometheus-L KrF laser driver baseline design excludes large EBELs because of their catastrophic failure modes, potentially serious impact on reactor operation if a failure occurs (owing to the 1% direct-drive target illumination uniformity requirement), and unproven reliability for a large number of high quality amplifier firings (~10^9).

6.5.1.2.3 **Excimer Laser Preamplifier (ELP)** - The purpose of the excimer laser preamplifier (ELP) is to amplify the relatively weak beamsplitter-divided beams from the ELMO to a level sufficient to drive the ELDs to their specified output energies. The specifications for the ELP are provided in Table 6.5.1-2 (with a possible future substitution of ArF).

It should be noted that there are 960 excimer laser amplifier chains which generate the ~5.9 MJ of energy directed into the 60 Raman accumulator cells (RACs). In addition, there are 60 excimer laser chains (using 60 ELPs and 60 ELDs) which drive the Stokes seed generators for the RACs.

Table 6.5.1-2 Prometheus ELP Specifications

Parameter	Nominal Value	Unit of Measure
Number of Units	1020	
Wavelength	248	nm
EDEL Mode Pulse Duration	270 (620, EBEL)	ns
Input Energy	0.04	J
Output Energy	4	J
Gain	100	
Polarization State	Linear	
Aperture	1x1	cm
Gain Length	200	cm
Output Fluence	4	J/cm^2
Anode Voltage	100	kV
Beam Current	1.6	kA
Fuel Pressure (Kr, F_2, Ar)	760	torr
Number of Firings between Failures	10^{10}	
EDEL Mode Input Intensity	0.16 (0.08, EBEL)	MW/cm^2
EDEL Mode Output Intensity	16 (8, EBEL)	MW/cm^2
Repetition Rate	5	Hz

ELP Excitation Design - In order for the excimer laser amplifier chains to function efficiently, all types must have similar pumping pulse durations, spectral outputs, etc. Thus the ELP excitation design is similar to that of the ELMO, ELD, and ELPA units. A further consideration which is pending is the substitution of ArF for KrF as possibly being more efficient if corresponding transmissive optics problems can be solved.

Depending upon whether the excimer laser technology is based upon electric discharge or e-beam excited excimer lasers, each of the excimer amplifier types will conform to one of these two general categories.

ELP Performance Characteristics - The ELP is a general purpose excimer laser preamplifier designed to increase power levels in the Prometheus excimer laser chains to levels achieve efficient power extraction from the laser amplifiers. Excitation pulse durations are selected to be appropriate for the type of excimer laser chain (EDEL or EBEL) and are corrected for amplifier saturation effects (associated with efficient energy extraction) in the excimer amplifiers producing a noticeable shortening of the output pulse durations.

6.5.1.2.4 Excimer Laser Driver (ELD) - The excimer laser driver (ELD) subsystems in each of the 960 beamlines amplify the beams from the ELPs to levels sufficient to drive the ELPAs to reach their specified output energies. Schematics of the locations of the ELDs relative to ELMO and the ELPAs are provided in Figure 6.5.1-3. Specifications for the ELD are provided in Table 6.5.1-3.

Table 6.5.1-3 Prometheus ELD Specifications

Parameter	Nominal Value	Unit of Measure
Number of Units	1020	
Wavelength	248	nm
EDEL Mode Pulse Duration	260 (570, EBEL)	ns
Input Energy	4	J
Output Energy	200	J
Gain	50	
Polarization State	Linear	
Aperture	10x10	cm
Gain Length	200	cm
Output Fluence	2	J/cm^2
Fuel Pressure (Kr, F_2, Ar)	760	torr
Number of Firings between Failures	10^{10}	
Anode Voltage	200	kV
Beam Current	40	kA
EDEL Mode Input Intensity	0.16 (0.08, EBEL)	MW/cm^2
EDEL Mode Output Intensity	8 (4, EBEL)	MW/cm^2
Repetition Rate	5	Hz

6.5.1.2.5 Excimer Laser Power Amplifier (ELPA) - The excimer laser power amplifiers (ELPAs) amplify the ELD beams to levels sufficient to drive the subsequent Raman accumulator cells. These amplifiers are primarily scaled-up versions of the ELDs with apertures increased from 5x5 cm to 30x30 cm and amplification length of 2 m. Schematics of the relative locations of the ELPAs relative to ELDs and the Raman accumulators are provided in Figures 6.5.1-3 and 6.5.1-4. The specifications for the ELPA are provided in Table 6.5.1-4.

Note that by arranging to have the total pressure in the ELPA ~1 atmosphere permits the amplifier windows to be thinner since the differential pressure can be nearly zero for quiescent amplifiers. (The dynamic overpressure is several atmospheres when the amplifiers are fired.) Similar conditions apply to the ELPs and ELDs, although the cost benefits for these smaller amplifiers is less.

Table 6.5.1-4 Prometheus ELPA Specifications

Parameter	Nominal Value	Unit of Measure
Number of Units	960	
Wavelength	248	nm
EDEL Mode Pulse Duration	250 (500, EBEL)	ns
Input Energy	200	J
Output Energy	6000	J
Gain	30	
Polarization State	Linear	
Aperture	30x30	cm
Gain Length	200	cm
Output Fluence	5.5	J/cm^2
Anode Voltage	300	kV
Current	3.3	MA
Fuel Pressure (Kr, F_2, Ar)	760	torr
Number of Firings between Failures	10^{10}	
EDEL Mode Input Intensity	0.7 (0.35, EBEL)	MW/cm^2
EDEL Mode Output Intensity	22 (11, EBEL)	MW/cm^2
Repetition Rate	5	Hz

A schematic of a possible pulsed power configuration for an EDEL version of the ELPA is shown in Figure 6.5.1-7. As indicated in the figure, maximum efficiency can be realized by locating the pulsed power Blumleins adjacent to the EDEL amplifiers. Although UV preionization grids are shown, this configuration could also be used for an e-beam sustained EDEL. Circulation of the hot gases from the ELPA will be discussed in Section 6.5.1.6. The 6 kJ output beams from each of these ELPAs are then directed into the Raman accumulator optical system.

6.5.1.3 <u>Raman Accumulator Subsystems</u> - Using a Raman laser subsystem duplicated 60 times, the ~6 kJ output beams from 4x4=16 ELPAs are directed into a 1.2x1.2 m-square aperture, 5-m long Raman accumulator cell (RAC) filled with ~1 amagat of D_2. For maximum conversion efficiency, the intended stimulated Raman scattering amplification process in the RAC is stimulated rotational Raman scattering (SRRS); more specifically, SRRS from the S(1) transition in H_2 or D_2. (Raman laser operation with D_2 has a slightly higher quantum efficiency than with H_2.) The required Stokes seed is derived from a local SRRS master oscillator, pumped with excimer laser light derived from a particular ELD chain, having identical spectral (and temporal) content as the 16 ELPA pump beams entering the RAC. This spectral matching of the Stokes seed to the 16 ELPA pump beams assures high Raman gain[9] even in the presence of relatively broad-band (~1 GHz) excimer pump beams. This results in efficient conversion of these 16 pump beams to generate the main square 1.2x1.2-m aperture 100 kJ Stokes output beam from the RAC. By injecting the pump beams into the RAC at an angle of 5° with respect to the RAC axis, an acceptable degree of pump[9,10,11] beam intensity averaging is achieved in the 5 m gain length, while not significantly reducing the Raman amplifier gain (see Section 4.2.1).

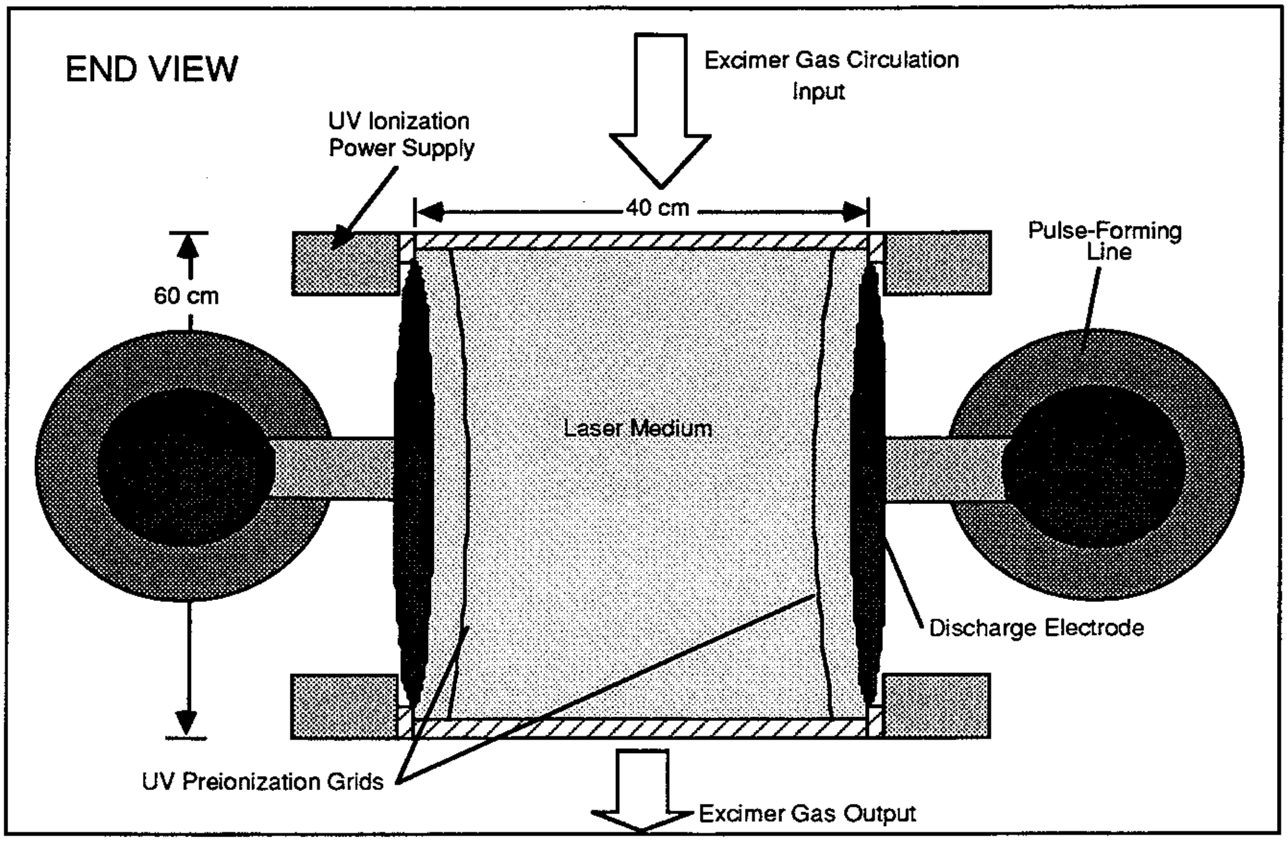

Figure 6.5.1-7 Pulsed power configuration for the EDEL version of the ELPA

A simplified schematic of the Raman Stokes seed generator designed to drive the Raman accumulator cell (RAC) is shown in Figure 6.5.1-8.

The 200 J output beam from the 17th ELD beam line is divided into a small 0.5 J pump beam and main beam (199.5 J). This small beam is directed into a local Raman oscillator with an output Stokes energy of 0.1 J. The beams (Stokes seed and main) rejoined at an angle relative to each other in the Raman preamplifier. The Raman Preamplifier output is a 30 J Raman Stokes seed at a wavelength of 251 nm (for KrF) or 196 nm (for ArF)). It is essential that the Raman seed have excellent beam quality to assure high quality beams on the DT target. The Stokes seed generator would include image-relayed spatial filter telescopes (not illustrated in the figure) to produce essentially diffraction-limited 1.2 m x 1.2 m beams for injection into the Raman accumulator.

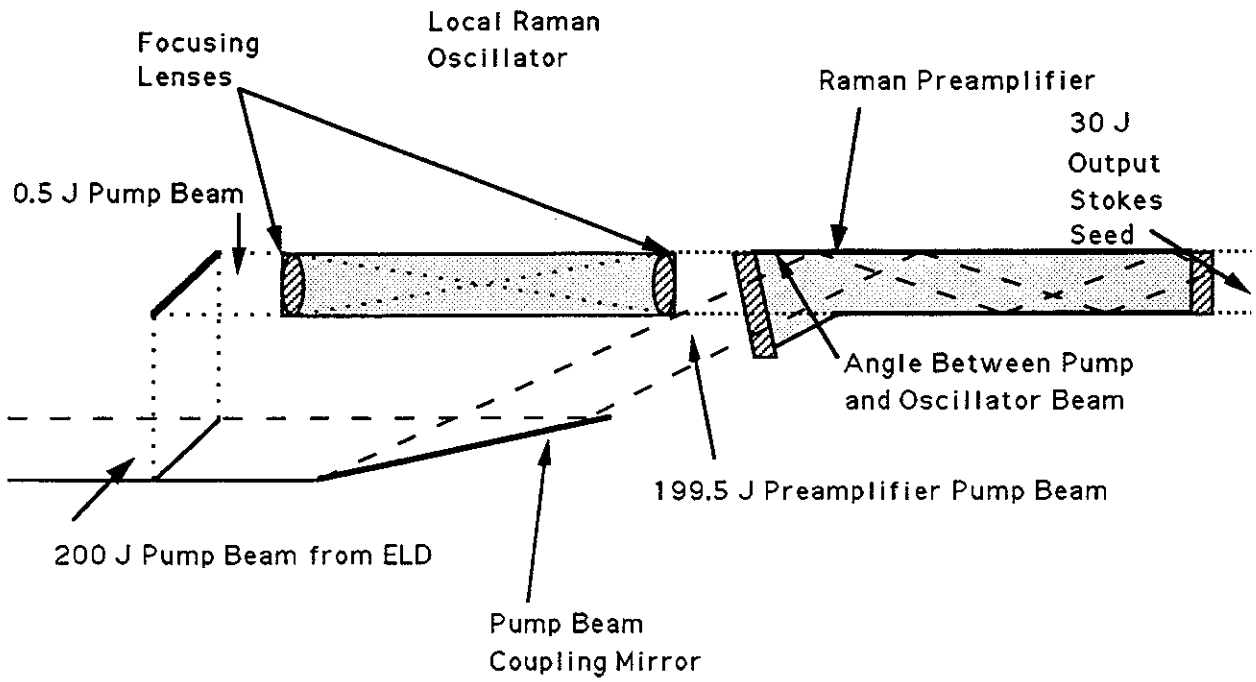

Figure 6.5.1-8. Each Raman accumulator subsystem consists of a local Raman oscillator (LRO), a Raman preamplifier, and a recollimation telescope generating 120x120 cm Raman Stokes seed beam of 30 J to drive the Raman accumulator cells.

To achieve good spectral match among the Raman oscillator and amplifier elements, the entire Raman conversion system operates at the same temperature and pressure. Characteristics of the Raman amplifier cells are summarized in Table 6.5.1-5.

Table 6.5.1-5 Common Raman Amplifier Specifications

Parameter	Nominal Value	Unit of Measure
Pump Laser Type	KrF	λ = 248 nm
Raman Medium	hydrogen	gas
Gas Density	~ 1	amagat
Transition #1	S(2)--S(0)	ΔE ~ 354 cm^{-1}
Quantum Efficiency #1	99.1 (KrF)	%
First Stokes Wavelength #1	250.2	nm
Transition #2	S(3)--S(1)	ΔE ~ 587 cm^{-1}
Quantum Efficiency #2	98.5 (KrF)	%
First Stokes Wavelength #2	251.6	nm
Pump Laser Type	ArF	λ = 193 nm
Transition #1	S(2)--S(0)	ΔE ~ 354 cm^{-1}
Quantum Efficiency #1	99.3 (ArF)	%
First Stokes Wavelength #1	194.3	nm
Transition #2	S(3)--S(1)	ΔE ~ 587 cm^{-1}
Quantum Efficiency #2	98.9 (ArF)	%
First Stokes Wavelength #2	195.2	nm

6.5.1.3.1 **Local Raman Oscillator** - The local Raman oscillator (LRO) generates a high quality Stokes seed that is amplified by the Raman preamplifier prior to injection into the Raman accumulator cell (RAC). The general construction of the LRO is shown in Figure 6.5.1-8. In this geometry, the 0.5 J pump beam is focused into a 200-cm long H_2 cell using a high quality lens of focal length, f ~ 100 cm. The gas pressure in the LRO cell is selected to be similar to the Raman preamplifier and RAC to achieve similar Raman bandwidth and gain coefficients (see Section 4.2.1). For an input pump with wavelength λ_{pump} of diameter d_b, having an energy E_p, a beam quality of ξ, and a pulse duration of τ_p, the intensity, I_{laser}, near the focus of the lens is simply:

$$I_{focus} = \frac{E_p d_b^2 \pi}{4\lambda_{pump}^2 f^2 \tau_p \xi^2} \qquad (6.5.1\text{-}1)$$

Using the values in Eq. 6.5.1-1 produces a pump intensity near the focus is ~3 GW/cm^2. The small angle, forward Raman gain, G_R, in H_2 under these circumstances is described by the expression:

$$G_R(\rho,\theta,\lambda) = \exp\left[g_R(\rho,\theta,\lambda) I_{focus}(\lambda) L(\lambda)\right] \qquad (6.5.1\text{-}2)$$

where $L(\lambda)$ is defined by

$$L(\lambda) = \frac{4\xi f^2 \lambda_{pump}}{\pi d_b^2} \qquad (6.5.1\text{-}3)$$

where g_R is the Raman gain coefficient, L_λ is the depth of focus of the lens, and I_{focus} is the intensity of the laser beam described by Eq. 6.5.1-1 above. Substituting values from Table 6.5.1-6 into Eq. 6.5.1-2 yields a result that the small signal Raman gain, G ~ 30 nepers or approximately 10^{13}. Under these circumstances, the Raman gain is sufficiently high that amplified spontaneous emission (ASE) is sufficient to saturate the Raman medium, yielding a 0.1 J pulse of Stokes radiation. The beam quality of the Stokes seed generated under these conditions is relatively good since the solid angle of the gas in which the seed is generated is relatively small. It is necessary, however, to spatially filter the seed further prior to amplification in the Raman preamplifier in order to improve the Stokes seed beam quality to be close to the diffraction limit. Care must be taken to assure that the LRO only generates the first Stokes order and that generation of all higher order Stokes outputs are strongly suppressed.

Typical values for the LRO parameters can be found in Table 6.5.1-6.

Table 6.5.1-6 Prometheus Local Raman Oscillator Specifications

Parameter	Nominal Value	Unit of Measure
Number of Units	60	
EDEL Mode Pulse Duration	250 (500, EBEL)	ns
Input Pump Energy	~0.5	J
Output Stokes Energy	~0.1	J
Conversion Efficiency	20%	
Polarization State	Circular	
Aperture	1x1	cm
Oscillator Length	3	m
Output Fluence	0.1	J/cm^2
Number of Conversions/Failures	10^{11}	
EDEL Mode Input Intensity	2 (1, EBEL)	MW/cm^2
EDEL Mode Output Intensity	0.4 (0.2, EBEL)	MW/cm^2
Repetition Rate	5	Hz

6.5.1.3.2 Raman Preamplifiers - The Raman preamplifiers increase the power of the Stokes seed generated in the LRO from 100 mJ to a level ranging from 30 to 50 J prior to injection into the RAC. A schematic of the relation of the Raman preamplifier relative to the LRO is shown in Figure 6.5.1-6. The general specifications of Raman preamplifiers are summarized in Table 6.5.1-7.

Table 6.5.1-7 Prometheus Raman Preamplifier Specifications

Parameter	Nominal Value	Unit of Measure
Number of Units	60	
Wavelength	249	nm
EDEL Mode Pulse Duration	250 (500, EBEL)	ns
Stokes Seed Energy	0.1	J
Input Pump Energy	~200	J
Output Stokes Energy	~30	J
Conversion Efficiency	15%	
Raman Cell Gain	300	
Polarization State	Circular	
Aperture	5x5	cm
Gain Length	3	m
Output Fluence	1.2	J/cm^2
Number of Conversions/Failures	10^{11}	
EDEL Mode Input Intensity	32 (16, EBEL)	MW/cm^2
EDEL Mode Output Intensity	4.8 (2.4, EBEL)	MW/cm^2
Repetition Rate	5	Hz

As indicated, the Raman preamplifiers are pumped with ~200 J pulses delivered by the 17th excimer amplifier chain (composed of an ELP followed by an ELD). The pump pulses are injected into the Raman preamplifiers at an angle in order to permit the intensity inhomogeneities present in the ELD pump beam to be averaged out in the Raman preamplifier, thereby permitting a very smooth Stokes seed to be delivered to the RAC.

6.5.1.3.3 <u>Raman Accumulator Cells (RAC)</u> - The Raman accumulator cells (RACs) perform the important task of combining the output beams from 16 ELP/ELD/ELPA laser chains into a single, 100 kJ beam having an aperture of 1.2 x 1.2 m. A simplified schematic of the Raman accumulator cells (RACs) is shown in Figure 6.5.1-9.

A diagram illustrating in more detail the proposed injection scheme of all 16 ELPA beams into the RAC can be found in Section 2.4. The general performance requirements for the Raman accumulator cells (RACs) are summarized in Table 6.5.1-8.

Many variables influence the conversion efficiency of a Raman accumulator. As shown in Figure 6.5.1-10, even for constant values of excimer laser intensity, variations in hydrogen gas density, angle of injection, and cell length play important roles in determining the cell conversion efficiency.

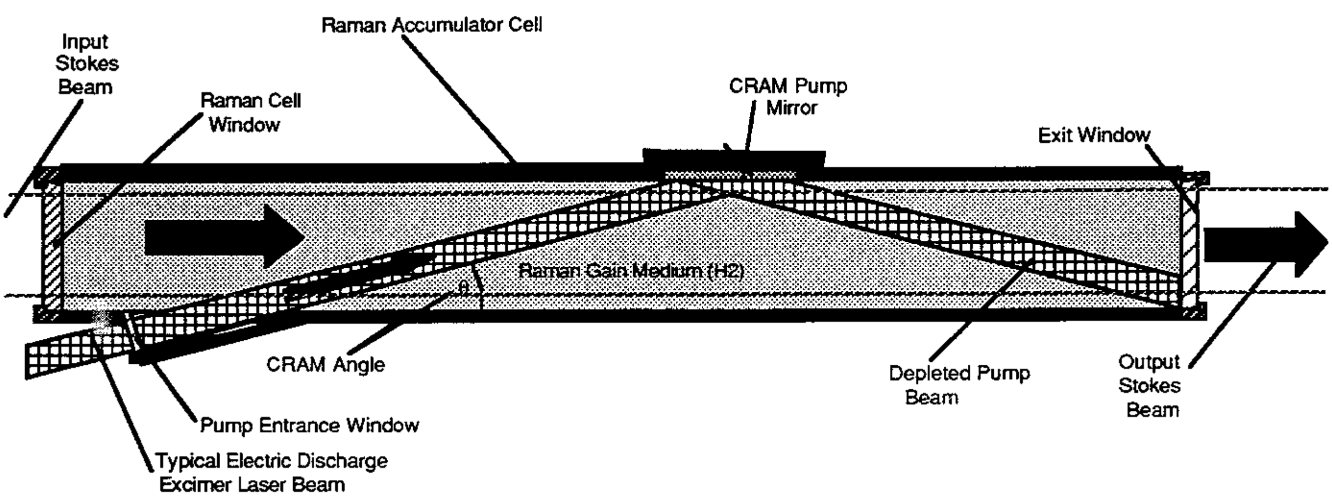

Figure 6.5.1-9 Injection of the Stokes seed into the Raman accumulator cell permits the efficient extraction of the excimer pump beams into a 100 kJ beam having an aperture of 1.2x1.2 m.

Table 6.5.1-8 Prometheus Raman Accumulator Specifications

Parameter	Nominal Value	Unit of Measure
Number of Units	60	
Wavelength	249	nm
EDEL Mode Pulse Duration	250 (500, EBEL)	ns
Stokes Seed Energy	30	J
Input Pump Energy	~96	kJ
Output Stokes Energy	~81	kJ
Conversion Efficiency	84%	
Raman Cell Gain	3000	
Polarization State	Circular	
Aperture	1.2x1.2	m
Beam Quality	1.2	xDL
Gain Length	6	m
Output Fluence	8	J/cm^2
Number of Conversions/Failures	10^{11}	
EDEL Mode Input Intensity	0.16 (0.08, EBEL)	MW/cm^2
EDEL Mode Output Intensity	8 (4, EBEL)	MW/cm^2
Repetition Rate	5	Hz

In order to avoid conversion of the first Stokes output to higher order Stokes components[9,10,11], Raman conversion efficiencies higher than 90% should be avoided. Thus, as indicated in Figure 6.5.1-10, the RAC cell should be ~250 cm in length for a hydrogen density of 1.4 amagat and a CRAM angle of 10° in order to avoid higher order Stokes components from being generated (using the converted first Stokes beam as a pump beam for the second Stokes, etc.).

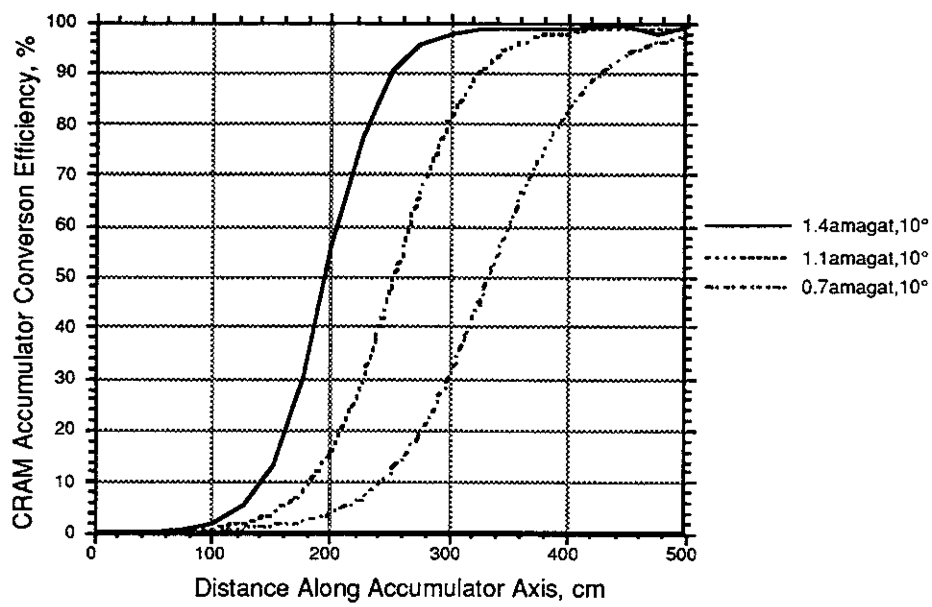

Figure 6.5.1-10 The RAC conversion efficiency is dependent upon the CRAM angle (example shown is 10°), hydrogen gas density (examples shown are 0.7, 1.1, and 1.4 amagats), and distance along the accumulator axis assuming a 5 GHz bandwidth, 250 nm pump beam, 100 kJ energy in 250 ns pulse duration.

The formal dependencies of the Raman gain on hydrogen density, CRAM angle, pump bandwidth, laser intensity, cell length, etc., were described in Section 4.2.1; the angular dependence of the Raman gain coefficient, g_R, is defined by the expression:

$$g_R(\theta,\lambda,\rho) = \frac{\alpha(\lambda,\rho)}{1+\xi(\lambda,\rho)\left[1+\psi(\lambda,\rho)\sin^2\left\{\frac{\theta}{2}\right\}\right]} \tag{6.5.1-4}$$

where θ is the angle between the pump and Stokes seed (α, ξ, ψ) are functions of the laser wavelength, λ, and hydrogen density, ρ. The Raman gain, G_R, on the other hand is given by the expression:

$$G_R(\theta,\lambda,\rho) = \exp\left[g_R(\theta,\lambda,\rho)\, I_{pump}(\lambda)\, L_{cell}(\theta)\right] \tag{6.5.1-5}$$

where I_{pump} is the intensity of the excimer pump laser beams, and $L_{cell}(\theta)$ is the length of the Raman cell. It is important to recognize that there are competing processes present in the RAC which must be controlled if the performance described in Figure 6.5.1-10 is to be realized. Some of these processes include higher order Raman conversion or generation of parasitic Raman oscillations parallel to the RAC axis (as discussed in Section 4.2.1 and illustrated in Eq. 6.5.1-1); the Raman gain coefficient for $\theta = 0°$ is significantly higher than for $\theta = 10°$). In general, if $G_R > 10^{10}$ for a Raman process (equivalent to 23 nepers of gain), superfluorescent oscillation may occur, depleting the available pump energy.

6.5.1.4 SBS Pulse Compressors - The SBS pulse compressors transform the relatively long (~250 ns pulses in the case of the EDELs or ~500 ns in the case of the EBELs) laser pulses from the RACs into complex pulse shapes. For direct-drive laser targets, these complex pulse shapes consist of a ramped precursor pulse of ~80 ns duration containing ~30% of the energy, followed by a main pulse having a ~6 ns duration with ~70% of the total pulse energy. Two examples of such a direct-drive pulse scenario are shown in Figure 6.5.1-11.

A SBS pulse compressor subsystem takes the roughly rectangular, 250 ns pulse from the RAC and generates a short, 6 ns main pulse illustrated in Figure 6.5.1-11. A long, 80 ns precursor pulse is derived from temporally inverting the depleted pump beam emanating from the SBS cell. These SBS processes are described below.

6.5.1.4.1 Generation of SBS "Seed" Beam - In a manner analogous to the Raman seed generator described in Section 6.5.1.3.1, the SBS pulse compressor seed is derived from the long duration pulse of the RAC. Henceforth, this long duration pulse from the RAC is referred to as the "SBS pump pulse." Using a method originally suggested by Mak,[12] the leading edge (i.e., the first 10 ns) of this SBS pump pulse is "chirped" or frequency-shifted by an amount equal to the Brillouin shift in the SF_6 gas used as the SBS gain medium. By varying the duration and modulation depth of the "chirped" signal on the leading edge of the SBS pump beam, significant control can be exercised over the shape and pulse duration of resulting compressed pulse.

6.5.1.4.2 Amplification of Short Duration Stokes "Seed" - This long SBS pump beam is then passed through a quarter-wave plate to convert the previously circular polarized light (needed in the rotational Raman accumulators) to linearly polarized light vibrating in the "p" polarization. The beam is then transmitted without loss through a dielectric polarizer, a second quarter-wave plate oriented to return the "p"-polarized beam to circular polarization, and then passed through a gas cell filled with approximately 2 amagat of SF_6. The length of this SF_6 cell is designed to be $L_{cell} = c\,\tau_{pulse}/2$. At the far end of the SBS cell a high reflectivity mirror is located which retro-reflects the incident pump beam directly back into itself. Since the leading edge of the SBS pump beam has been frequency-shifted by the "chirper" by an amount equal to the SBS shift in SF_6, the leading edge of the SBS pumping pulse therefore serves as the SBS Stokes "seed" beam, and the frequency-shifted photons on the leading edge of the pump pulse experience high optical gain[13] as these photons propagate back

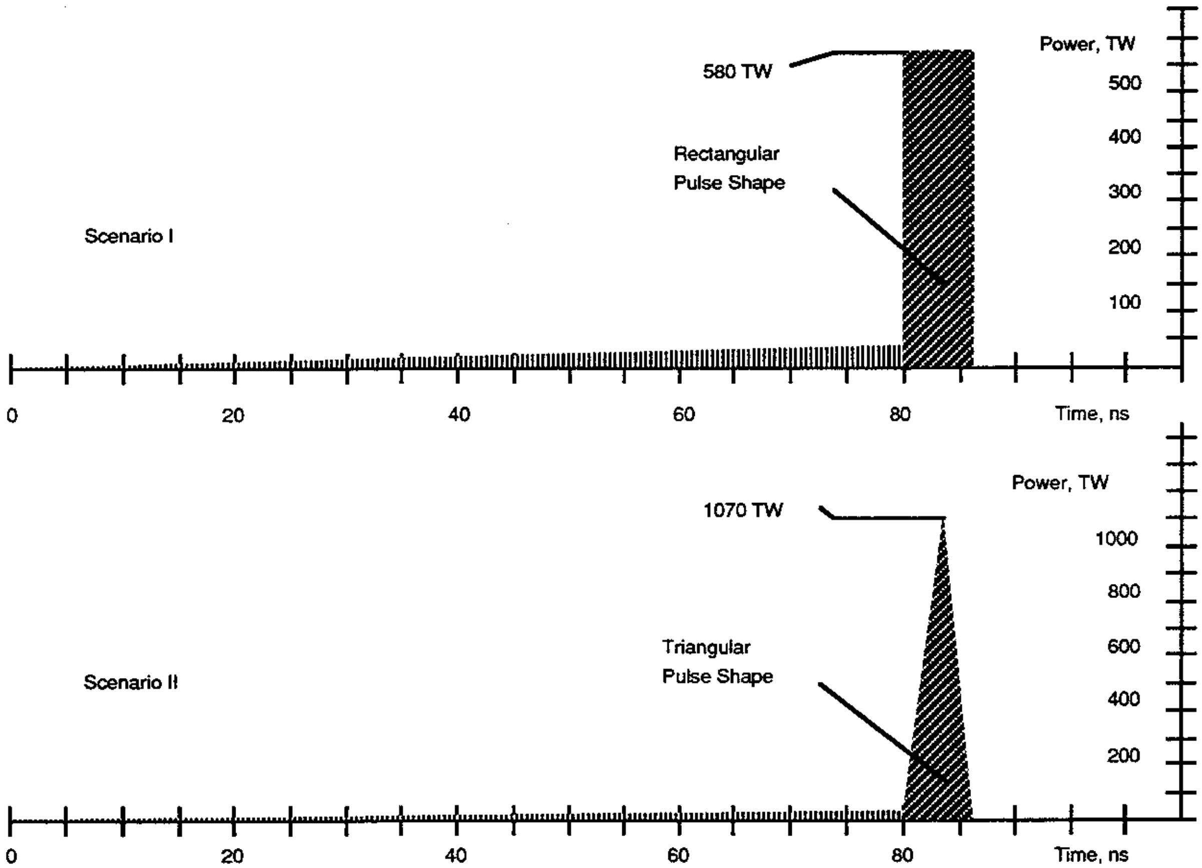

Figure 6.5.1-11 The complex temporal shape of the direct-drive laser driver pulse consists of a ramped, 80 ns precursor pulse followed by a short, 6 ns main pulse.

through the volume of the SF_6 gas "pumped" by the incoming beam. Assuming that the temporal pulse shape of the SBS pump beam is rectangular, the SBS gain, G_{SBS}, of the pulse compressor is given by the expression:

$$G_{SBS}(\rho, \Delta\nu, t) = \exp\left(g_{SBS}\left[\rho, \Delta\nu_{pump}\right] I_{laser}(\Delta\nu, t) L_{cell}\right) \qquad (6.5.1\text{-}6)$$

where g_{SBS} is the Brillouin gain coefficient, I_{laser} is the intensity of the SBS pump beam, and $L_{cell} = c\ \tau_{pulse}/2$ is the effective gain length of the SBS pulse compressor. Typical values for G_{SBS} in SF_6 for 100 kJ RAC pulses of 250 ns duration are 10 nepers, or ~2000. The SBS gain coefficient, $g_{SBS}(\rho,\ \Delta\nu_{pump})$ is primarily a function of the gas density, ρ, and the bandwidth of the pump laser, $\Delta\nu_{pump}$

The physical process of SBS differs from that of Stimulated Raman Scattering (SRS) in that the scattering of incident laser photons from sound waves in the SBS medium occurs, as compared with the scattering of light from molecular energy states as the basis of the SRS process. Since the difference in frequency between the excimer laser, ν_{laser}, and the Stokes seed, ν_{SBS} is simply the Doppler shift, $\Delta\nu_D$, suffered by the pump photons when scattered from the moving density waves in the Brillouin gain medium. Thus, $\Delta\nu_D = 2\nu_{laser}v/c$ (where v is the sound speed in the SBS medium and c is the speed of light), the quantum efficiency for the SBS process defined in Eq. 6.5.1-6 can be very high, ξ ~ 100%.

The Brillouin gain coefficient, g_B, is defined by the relation:[13]

$$g_B = \frac{k_s^2 \gamma_e^2}{n c v_s \rho \Gamma_B} \qquad (6.5.1\text{-}7)$$

where k_s is the wave vector of the Stokes beam, γ_e is the electrostrictive coefficient (of the SF_6 SBS gain medium), n is the refractive index, c is the speed of light, v_s is the speed of sound in the gas, ρ is the density, and Γ_B is the spontaneous Brillouin line width.

Building upon the work of Mak,[12] et al., in Russia, we have analyzed the case in which the leading edge of the long, 250 ns (or 500 ns for an EBEL) excimer laser pulse is electronically chirped in frequency by an amount equal to the SBS seed frequency, $\Delta\nu_{SBS}$, and then ramped in modulation depth to encourage the generation of pulses >1 ns duration, we then have a very flexible method of generating a variety of output compressed pulse shapes in a single non-linear, self-seeding, pulse compressor. A schematic of the SBS pulse compression concept is shown in Figure 4.2.1.2-12.

The short, ~10 ns "chirped" leading edge of the retro-reflected pump beam is amplified by the SBS gain, G, until it extracts most of the pump beam energy. With a second passage through the quarter-wave plate, the "p"-polarized beam is converted to an "s"-polarized beam, and reflected from the large aperture dielectric polarizer to the electro-optical switchyard and delay line. A schematic of this self-seeded SBS pulse compressor geometry is shown in Figure 6.5.1-12.

Details regarding the variety of short pulse shapes that can be generated by varying the shapes of the "chirped" leading edges of the input pump pulses can be found in Section 4.2.1. A diagram of this pulse compression process is shown in Figure 6.5.1-13.

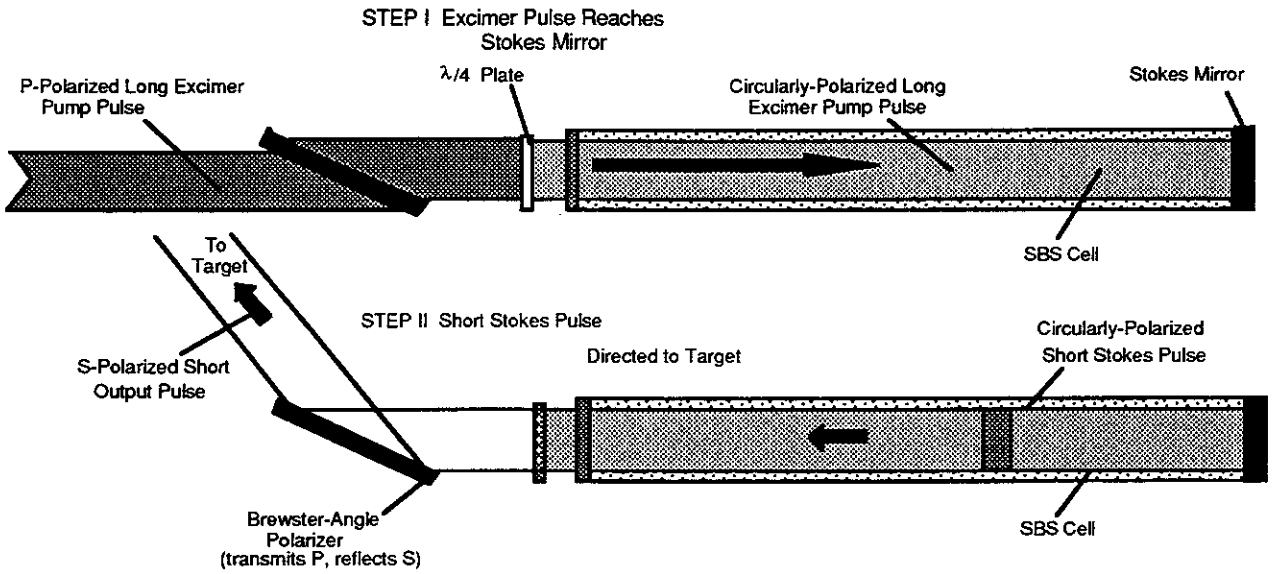

Figure 6.5.1-12 By frequency-"chirping" the leading edge of the SBS pumping pulse and reflecting it back upon the incoming pulse within an SF cell, it is possible to compress the RAC output pulse from 250 ns (or 500 ns) down to short pulse durations.

6.5.1.4.3 <u>Precursor Pulse Generation</u> - As mentioned previously, the SBS cell inefficiently generates compressed pulses as long as 6 ns. As a consequence of this inefficiency, approximately 60 to 70% of the pump beam is converted to the main 6 ns pulse, with 30 to 40% of the pump pulse being unconverted. As it turns out, these energy ratios of the long, depleted pump to the short main pulse are very similar to the required ratios for direct-drive target illumination set forth by the TWG. However as generated in the SBS pulse compressor, the short, 6 ns pulse precedes the long, depleted pump pulse. Accordingly, in order to generate the long duration precursor pulse from the depleted pump beam, it is necessary temporally to invert the short, 6 ns main pulse, from the long pulse. A schematic of how this can be accomplished is illustrated in Figure 6.5.1-14.

As indicated in Figure 6.5.1-14, the combined main short pulse and the long depleted pump beam emanating from the SBS pulse compressor cell enter into the pulse inverter optical system. This system applies a half-wave voltage to the large aperture Pockels cell, thereby changing the polarization of the short pulse from "p" to "s." The dielectric polarizer then reflects the short pulse into an optical delay line of length $L = c\tau_{laser}/4$ bisected with the dielectric polarizer. Immediately after the arrival of the short pulse, the half-wave voltage is removed from the Pockels cell, allowing the long duration, depleted pump beam to pass without loss through the dielectric polarizer. A quarter-wave plate located in the first arm of the delay line then converts the "s"-polarized short pulse into a

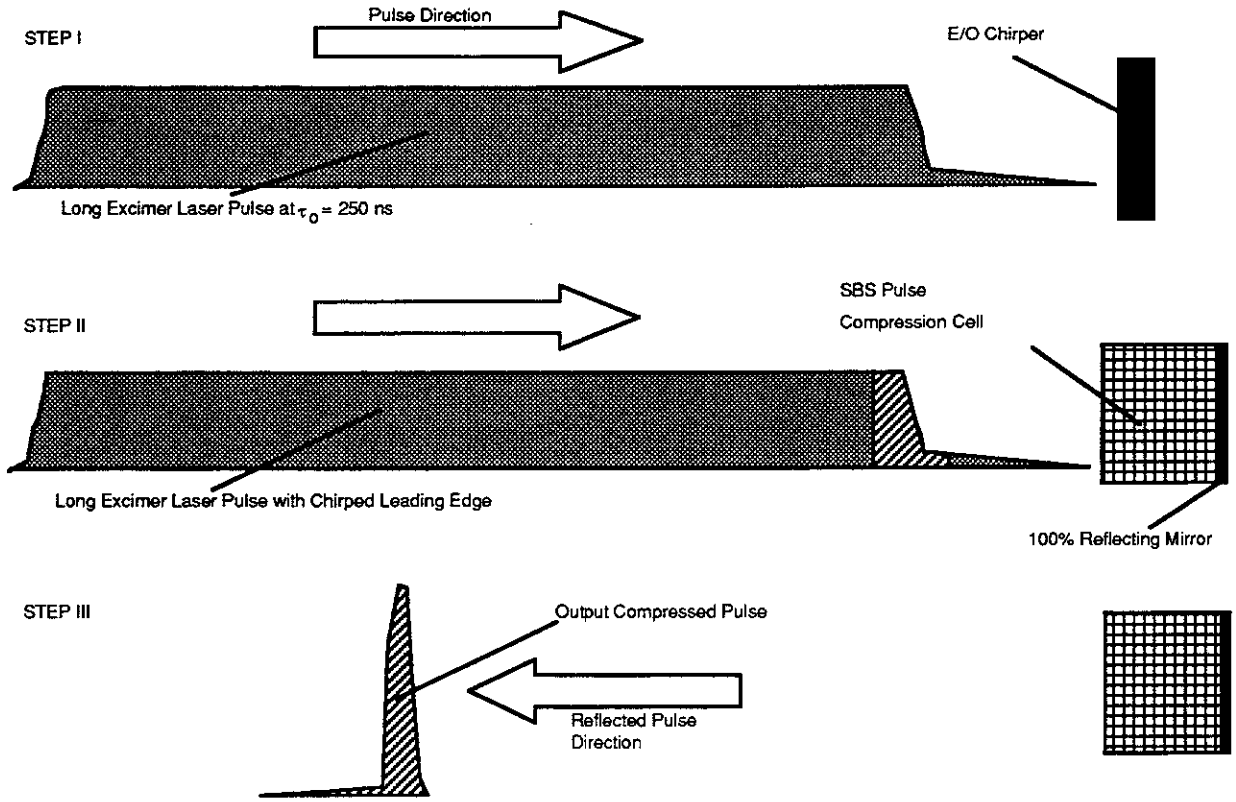

Figure 6.5.1-13 Pulse compression in the SBS pulse compressor.

"p" polarized wave which then transmits through the polarizer to the second delay line arm. Here a second quarter-wave plate converts the "p" -polarization back to "s"-polarization where the short pulse is finally reflected by the dielectric polarizer back into the main beam line, delayed by a time t = τ_{pulse}. The primary problem with this technique is that the pulse shape of the depleted pump beam from the SBS cell starts out at a relatively high level and ramps down (see Section 4.2.1).

An additional precursor pulse-shaping technique could be implemented if fast, large aperture Pockels cells are developed. A schematic of such a sample electro-optical switchyard technique is shown in Figure 6.5.1-15.

As shown in Figure 6.5.1-15, the SBS pulse compressor cell first generates the short, 6 ns main laser pulse, followed by the long, ~150 ns duration depleted pump beam. The first Pockels cell inverts the order of the short and long pulses, and the second (rapid rise-time) Pockels cell inverts the head and tail of the depleted pump beam to achieve a ramped precursor pulse shape.

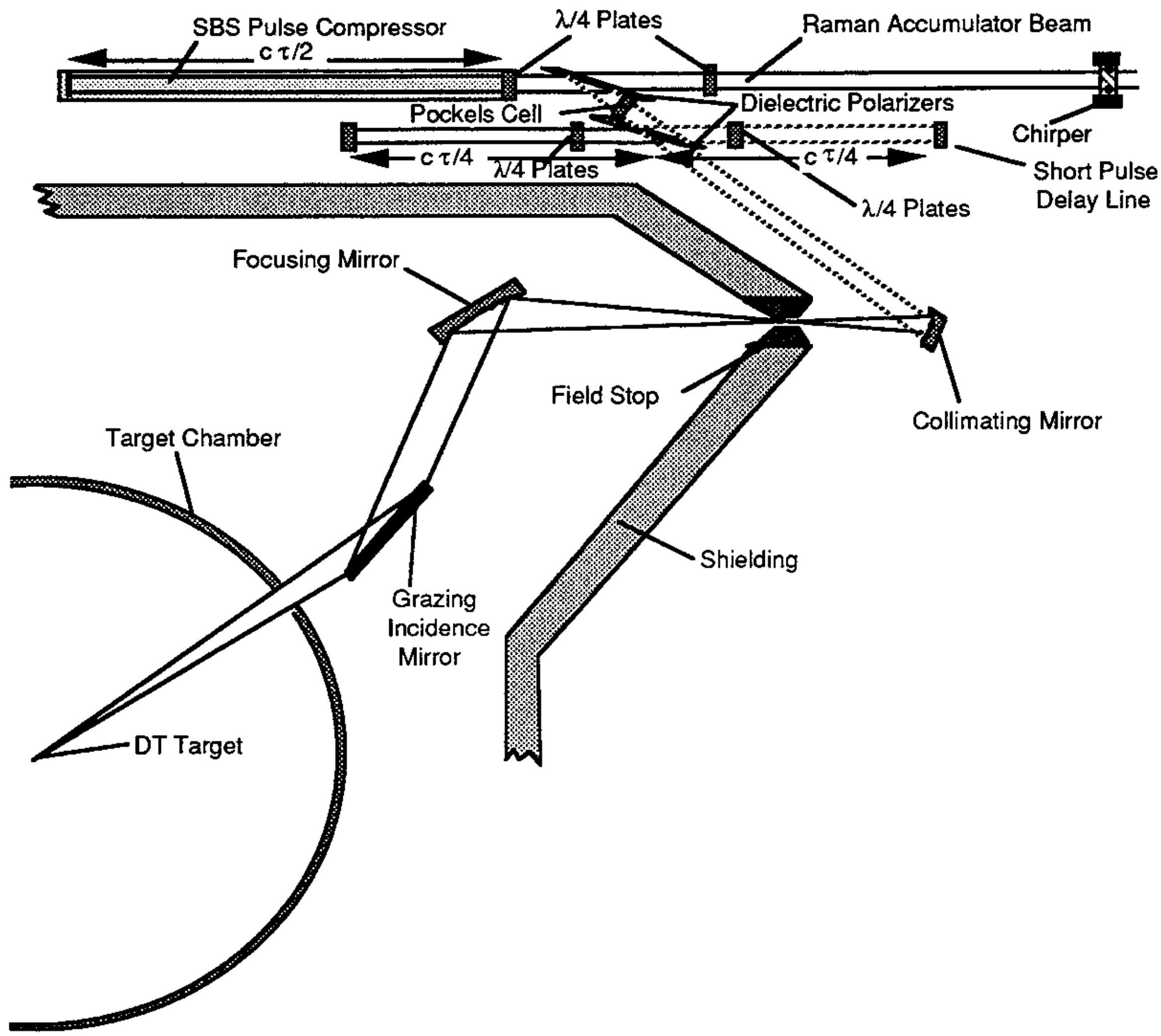

Figure 6.5.1-14 By use of a large aperture Pockels cell and a delay line, the short main pulse and long precursor pulses are temporally inverted.

SBS Pulse Shapes - Calculations were carried out for both EBEL (500-600 ns) and EDEL-pumped (250 ns) NLO pulse accumulator and compressor systems. As discussed above, the longer (~500 ns) EBEL pulses required a proportionally longer SBS cell ($L = c\,\tau_{pulse}/2$) than the shorter EDEL pulses. However, SBS conversion efficiencies >50% could be achieved with the longer EBEL pulses with SF_6 densities of ~1 amagat. An example of the variety of output pulse shapes that could be generated for an EBEL-converted Raman pump beam is shown in Figure 6.5.1-16.

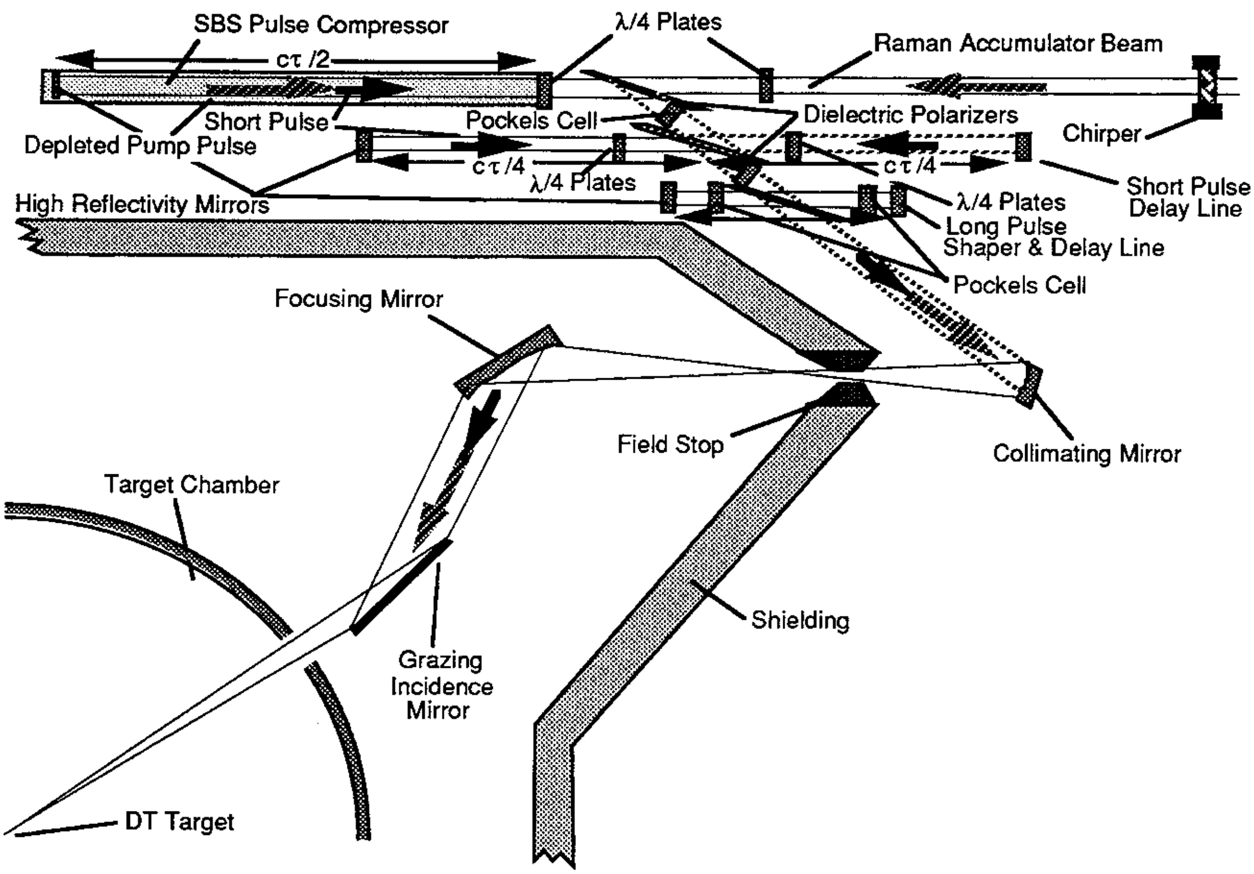

Figure 6.5.1-15 With fast Pockels cells and additional delay lines, additional temporal tailoring of the pulse shape is possible.

Similar results were obtained for the EDEL-pumped RAC case for which the pulse duration was ~250 ns. There was, however, insufficient SBS gain in the SF_6 gain medium to achieve high SBS conversion efficiencies with 1 amagat of SF_6 density. As a consequence, the density of SF_6 was increased to 2 amagat. The resulting pulse shapes as a function of the SBS "chirper" seed ramp ratios (see Section 4.2.1 for a discussion of the SBS "chirper" pulse ramp techniques) were calculated and the results are shown below in Figure 6.5.1-17 for a 248 nm pump, 5 GHz bandwidth, 1 m x 1 m aperture, and a 120 kJ input energy.

A laser designer does not have unlimited freedom in selecting different ramp ratios. The SBS pulse compression efficiency depended upon the ramp ratios, as shown in Figure 6.5.1-18.

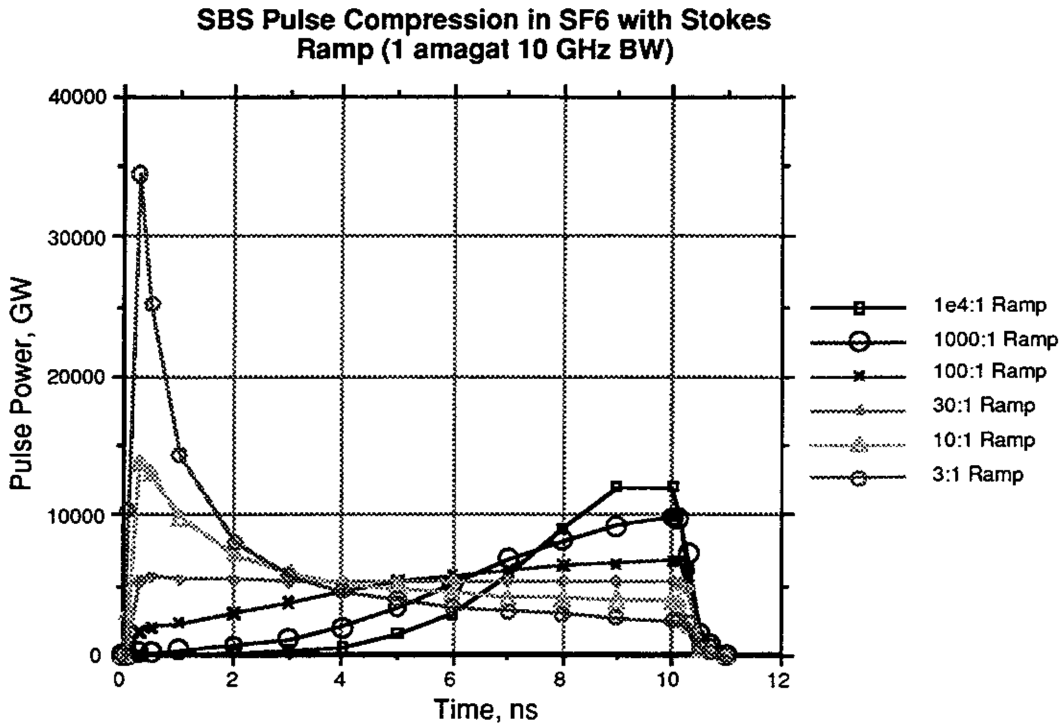

Figure 6.5.1-16 A variety of compressed pulse shapes could be achieved using a 600 ns Raman pump beam, 100 kJ energy, 1 amagat SF_6 density, and the indicated Stokes seed ramp ratios.

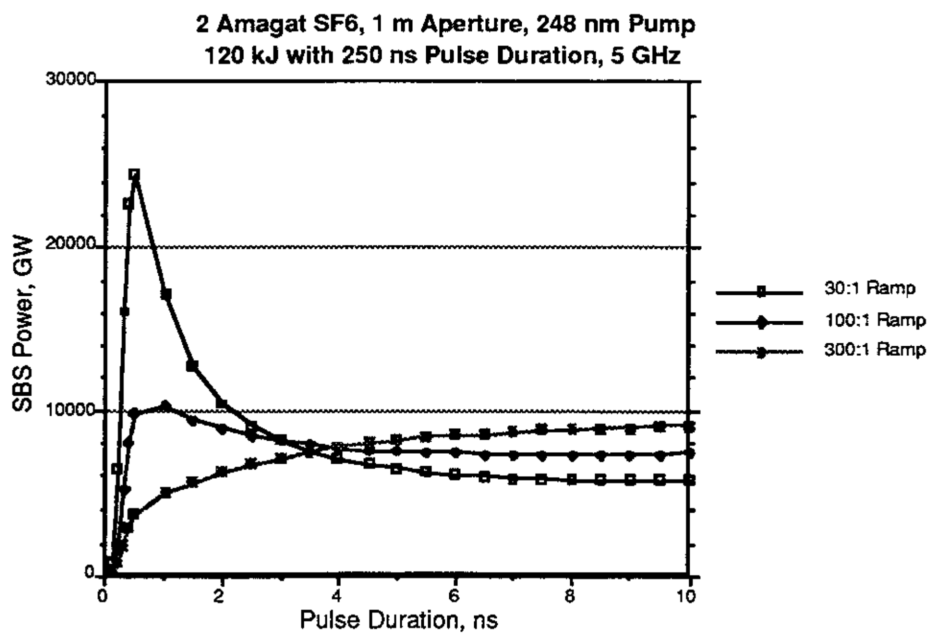

Figure 6.5.1-17 Further compressed pulse shapes can be generated using a 250 ns Raman pump beam at 250 nm, 120 kJ of energy, 2 amagat SF_6 density, 1x1 meter aperture and the indicated Stokes seed ramp ratios.

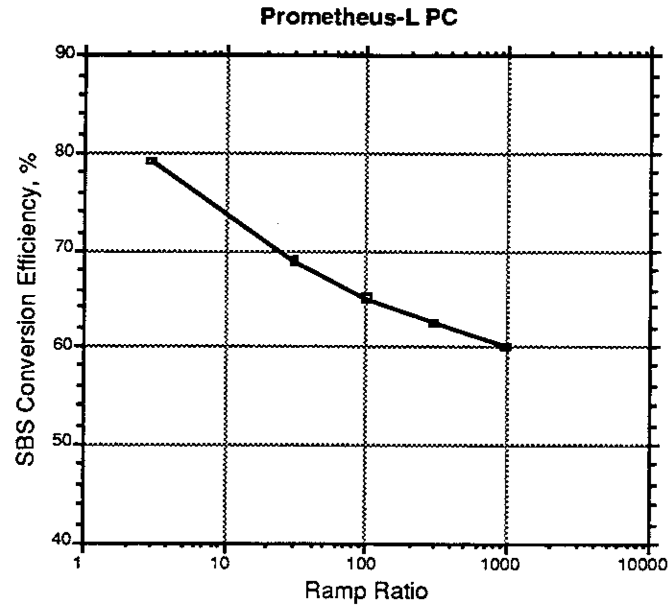

Figure 6.5.1-18 The SBS pulse compressor efficiency for 5 GHz 250 ns 120 kJ Raman pulses at 250 nm decreases as the Stokes seed ramp ratio increases.

As a consequence of design tradeoffs, an optimum pulse shape for the compressed main laser pulse can then lead to an optimization of the SBS pulse compressor conversion efficiency for the conditions necessary to generate the optimum pulse shape.

Temporal shapes of the depleted RAC pump beams emerging from the SBS compressor cells are also of interest since these pulses may be utilized elsewhere in the laser driver optical systems. These depleted pump pulses from the SBS cell remain of long duration and may be used as pump beams in a second SBS pulse compression stage or, if large aperture Pockels cells are developed, the depleted pumps can be electro-optically switched to generate a precursor pulse for the direct-drive target irradiation scheme.

As shown in Figure 6.5.1-19, the long RAC pulses (generated in the case of EBEL pumps) ramp down from ~190 GW to ~5 GW over the ~500 ns duration of the RAC pulse.

Similar results are obtained for the shorter pulse, EDEL-pumped RAC case. As shown in Figure 6.5.1-20, the temporal development of the depleted RAC pulse is illustrated for SBS "chirper" ramp ratios of 300:1 through 30:1.

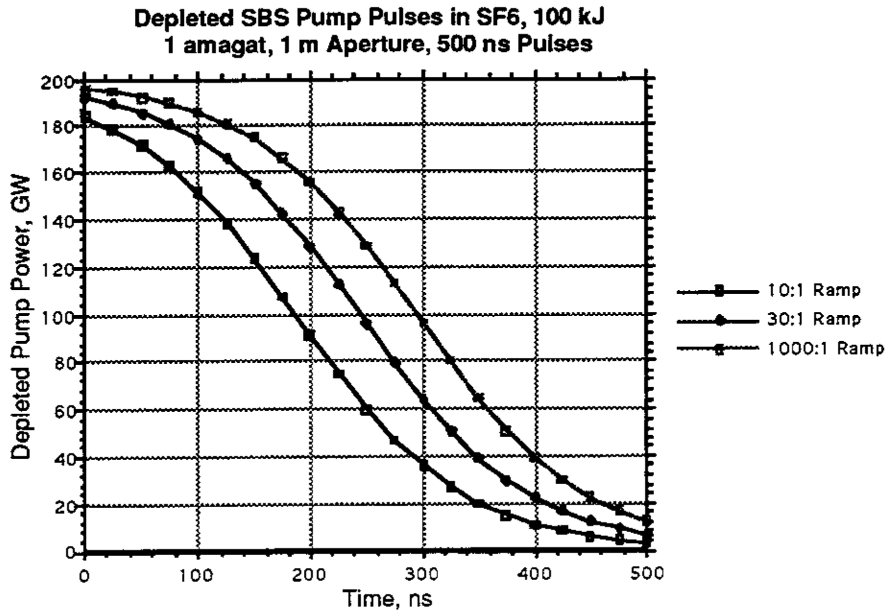

Figure 6.5.1-19 Temporal developments of depleted pump pulses emerging from SBS pulse compressor for 5 GHz, 100 kJ, 500 ns RAC pulses in 1 amagat of SF_6, 1x1 m apertures.

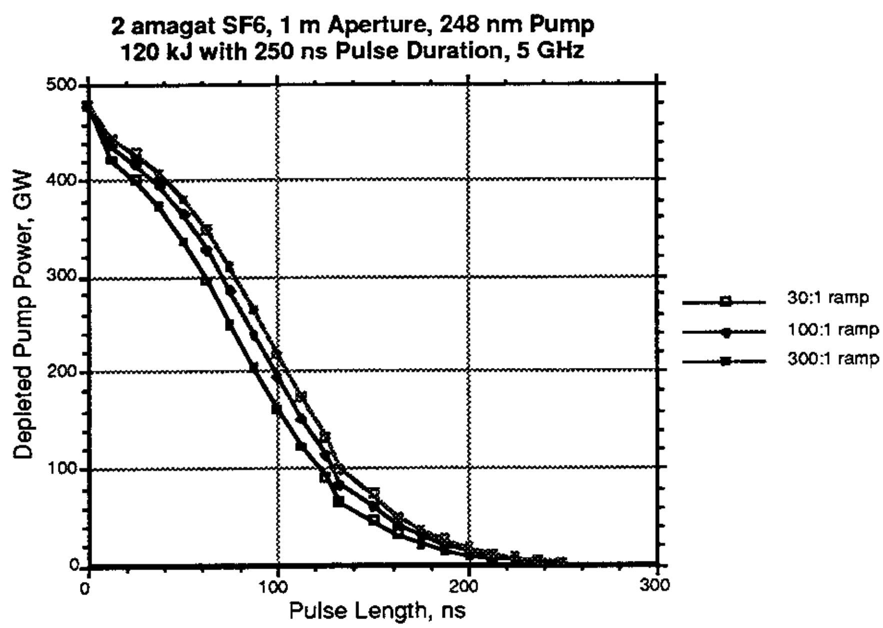

Figure 6.5.1-20 Temporal developments of depleted pump pulses from SBS pulse compressor for 5 GHz, 120 kJ, 250 nm pump, 250 ns pulse duration RAC pulses in 2 amagat of SF_6.

These are the pulse shapes which would need to be manipulated by the electro-optical switchyard depicted in Figures 6.5.1-14 and 6.5.1-15.

6.5.1.5 Excimer Laser Gas Flow System - As noted in Section 6.5.1.1, the overall efficiencies of the excimer laser amplifiers are predicted to be in the range of 12-15%. If the pulsed power efficiency is ~80%, then approximately 60% of the excimer laser pumping power will appear in the form of heat in the excimer laser fuel mixture gas. These estimates are summarized in Table 6.5.1-9, assuming that the power being fed to the laser driver is 250 MW.

Table 6.5.1-9 Energy Distribution in Excimer Laser Pumping

No.	Excimer Amplifier Component	% Power	Power (MW)
1	Output Photons	12-15%	30-40
2	Pulsed Power	20%	50
3	Excimer Gas	60%	150
4	Cooled Electrodes	3%	8
5	Cooled Amplifier Shell	2%	5

Each ELPA produces an average optical power of 30 kW (6 kJ at a 5 Hz rate) and, assuming a 12% efficiency, would be supplied with a power ~240 kW of which 60% (144 kW) would end up as heat in the excimer gas. Since the principal gases in the excimer laser are argon and krypton (the concentration of fluorine is only a few percent), the heat capacity of the excimer fuel is simply $C_V = 3/2\ R$. The volume, V_a, of each of the ELPAs is 30x30x200 cm, or $V_a \sim 180$ liters which corresponds to 8.04 moles at standard temperature and pressure (STP).

6.5.1.6 Laser Driver Optical Subsystems - A wide variety of optical subsystems which are crucial to the operation of the Prometheus laser driver. Several were previously described, such as the beamsplitter array in conjunction with the ELMO and the electro-optical switchyard. A number of these optical subsystems are integrated with the laser driver computer control system to permit real-time adjustments on the performance of the laser system. A summary of the elements comprising the Prometheus laser driver optical subsystems is provided in Table 6.5.1-10.

Table 6.5.1-10 Excimer Laser Optical Subsystems

No.	Optical Subsystem Component	Function	Approximate Quantity
1	Beamsplitter Array Mirrors	Generate Beam Multiplicity	1000
2	Oscillator Beam Detectors	Measures ELMO Power	10
3	Amplifier Coupling Mirrors	Deflects Beam Directions	8000
4	Recollimating Telescopes	Matches Amplifier Diameters	1900
5	Raman Seed Beamsplitters	Feeds Raman Oscillator	100
6	NLO Windows	NLO Cell/Atmosphere Barriers	240
7	Quarter-Wave Plates	Converts Linear Polarized to Circular	120
8	Spatial Filter Telescopes	Improves Seed Beam Quality	60
9	LA Image Relaying Telescopes	Eliminates Egg-Crate Diffraction	120
10	Amplifier AR-Coated Windows	Excimer/Atmosphere Barriers	6000
11	Large Aperture (LA) Mirrors	Deflects Beam Directions	120
12	Segmented NLO Windows	NLO Cell/Atmosphere Barriers	240
13	LA Electro-Optical "Chirper"	Generates SBS Seed	60
14	LA Quarter-Wave Plates	Converts Linear Polarized to Circular	360
15	LA Pockels Cells	Rapidly Changes Polarized State	120
16	LA Delay Line Mirrors	Reflects Beams at Normal Incident	240
17	LA Dielectric Polarizers	Reflects "s"-Polarized Beams	180
18	LA Collimating Mirrors	Focuses Beams Through Shield	60
19	Alignment Detector Array	Tracks Reflection from Target	60
20	Holographic Alignment System	Locates Target Precisely	3
21	Pulse Shape Monitors	Measures Output Pulse Shape	60
22	Back-Reflected Calorimeters	Measures Energy Missing Target	60
23	LA Focusing Mirrors	Focuses Beams on Target	60
24	Plasma Shutters	Blocks Retro-reflected Light	60
25	LA Grazing Incidence Mirrors	Reflects Focused Beams	60

A schematic diagram of the operational layout of the beamsplitter array can be found in Figure 6.5.1-2. Although space does not permit a thorough discussion of each of these optical subsystems here, some of the more important are described in the following sections.

6.5.1.6.1 **Laser Beam/Target Alignment System** - A key element in the Prometheus-L laser driver system is the laser beam/target alignment system. This system senses the positions of the moving DT target as it moves through the target chamber on its way to the location where all 60 laser beams are pointed. This is a difficult challenge because the laser/target alignment system contains sensitive sensors which can easily be damaged by the thermonuclear burn of the DT fuel pellet. As a consequence, a system of fast shutters will be required to protect the sensitive sensors in the 100 ms time following the DT target implosions. A simplified schematic of one of the target position sensors in the laser beam/target alignment system is shown in Figure 6.5.1-21.

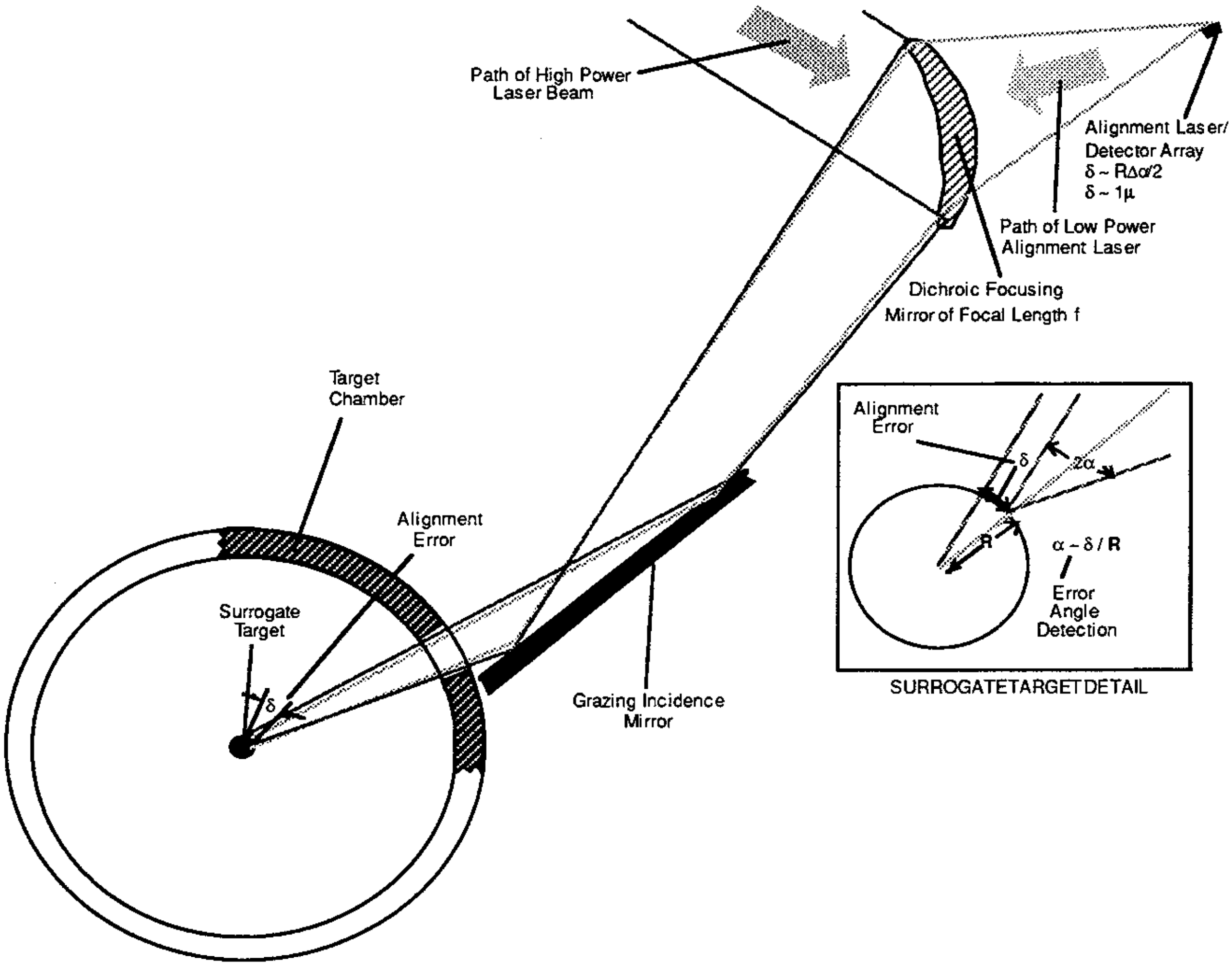

Figure 6.5.1-21 By utilizing a figured meniscus dichroic focusing mirror, it is possible to image the shine shield onto a highly magnified CCD array.

As indicated, it is recommended that the DT target have a "shine-shield" to assist the laser beam alignment system in tracking the target. Use of a holographic alignment system for the target permits very precise measurement of target positions as it moves through the target chamber.

6.5.1.7 Final Optics - The Prometheus-L target focusing scenario involves 60 beamlines using ~ 1 m diameter optics located 30 m from the target (20 m distance to the GIMM and an additional 10 m to the focusing mirror). A schematic of the three major elements in the Final Optical Train are shown in Figure 6.5.1-22.

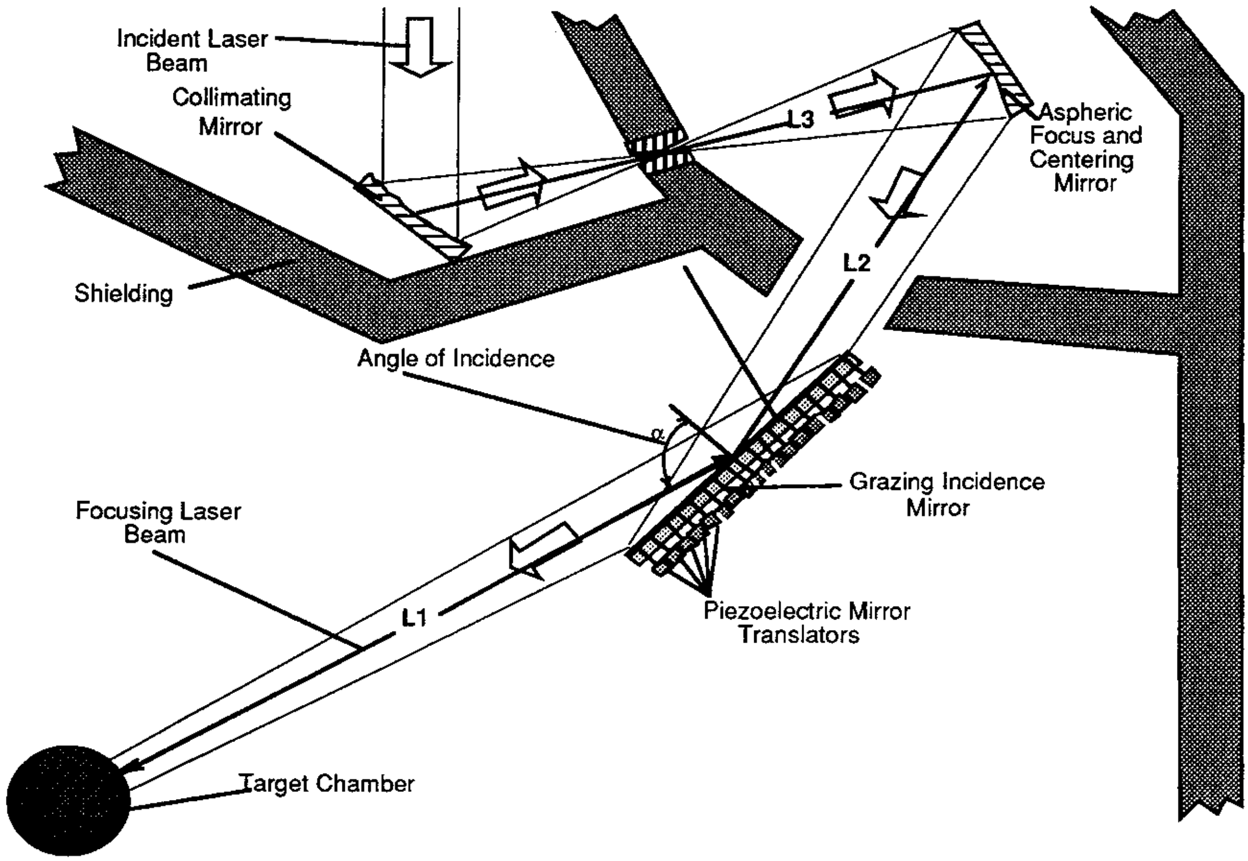

Figure 6.5.1-22 The incident beam from the E/O Switchyard is focused through and shielding by the collimating mirror, refocused by the focusing mirror, and beam directed onto the target by the grazing incidence mirror.

The grazing incidence mirror is shown with piezoelectric mirror translators for correcting neutron-induced neutron swelling. (These mirror adjustment devices are shown for illustration purposes only. Piezoelectric translators often show hysteresis effects and are prone to neutron damage.)

6.5.1.7.1 Collimating Mirror - The collimating mirror focuses the beam through the shielding to the focusing mirror. This permits a significant reduction in neutron fluence leaking through the primary shielding.

6.5.1.7.2 **Focusing Mirror** - The focusing mirror images the laser beam onto the DT target. Different scenarios are appropriate, depending upon whether the target is a direct-drive (DD) or indirect-drive (ID). The predicted far field focal spot size, d_{focus}, on the target is given by the expression:

$$d_{focus} = \frac{4\xi\lambda f_m}{\pi D} \qquad (6.5.1\text{-}8)$$

where λ is the laser wavelength (248 nm), D is the effective aperture of the focusing mirror (~1 m), f_m is the mirror focal length (~20 m), and ξ is the beam quality (~1.1). Substituting these values into Eq. 6.5.1-4 produces a value of $d_{focus} = 7\ \mu m$. Smaller spot sizes can be achieved for smaller values of λ (i. e., ArF at λ = 194 nm), f_m or for larger values of D.

Laser focal spot sizes this small are not of particular interest for direct drive targets with diameters of ~0.6 cm. However, this ability to focus the laser beams down to dimensions on the order of 10 microns is very interesting for indirect drive targets. A somewhat different illumination geometry would be likely—two-sided target irradiation with 30 beams per side arranged in 50° cones or sets of cones.

In addition, this mirror can be constructed to perform alignment tasks if properly figured and equipped with dichroic coatings (see Section 6.5.1.7.4).

A key issue associated with all of the optics in the laser chain is the optical damage threshold, Φ_o. The particular case considered here is that of the optical train consisting of the focusing mirror and the GIMM.

For an assumed total energy delivered to the target, E_{laser} = 5 MJ, each beamline spreads approximately 100 kJ over an area of 1.2 m x 1.2 m or ~ 1.44×10^4 cm^2. At normal incidence, the resulting optical fluence Φ ~ 7 J/cm^2. This fluence level is comparable with the current industry definitions for "optimistic" (Φ_{max} = 8 J/cm^2) and "conservative" (Φ_o= 3 J/cm^2) limits used for dielectric-coated high reflectivity (HR) mirrors in the ultraviolet using advanced coating technology. Higher values can be expected in the year 2030 if technological development occurs to improve the damage threshold of UV mirrors. If the angle of incidence of the laser beam is θ, then the effective fluence on the mirror is reduced by a factor of cos θ. If the damage threshold cannot be increased by coating manufacturers and if the cosine factor is insufficient, it may be necessary to increase the mirror aperture somewhat to provide an adequate mirror damage safety margin.

6.5.1.7.3 __Grazing Incidence Metal Mirrors (GIMMs)__ - As shown in Figure 6.5.1-22, the initial 1.2 m diameter for the laser beam at the focusing mirror decreases geometrically (down to 0.8 m diameter) at the GIMM (for a 10 m separation between the focusing mirror and the GIMM). Significant optical flux reductions are possible if grazing incidence mirrors are used as final turning mirrors since, for $\theta = 80°$, the cosine factor is ~5.75, reducing the fluence to ~3 J/cm^2. The optics designer must be cautious, however, since there are other damage mechanisms which may degrade grazing incidence mirrors. (Especially, particles lying on the optical surface experience the full laser intensity.)

This geometrical factor advantage of GIMMs carries over into reducing neutron fluence (and concomitant damage) as well. Additional work needs to be performed on the coatings for GIMMs to permit them to have damage thresholds higher than 3 J/cm^2 (assuming 6 ns pulse durations). The GIMM will be sized appropriately to assure that it will survive laser irradiation. A schematic illustrating the location of the GIMM is shown in Figure 6.5.1-22.

6.5.1.7.4 __Laser Beams Propagation Through Target Chamber Atmosphere__ - A variety of non-linear processes arising from residual gases in the target chamber can interfere with the delivery of the laser beam to the target. Non-linear processes depend upon the densities and compositions of the residual gases (as well as the laser beam intensity); therefore care must be taken to assure that their collective influences are negligible. Non-linear processes include: (1) laser-induced gas breakdown, (2) stimulated Raman scattering, (3) stimulated Brillouin scattering, and (4) multi-photon scattering. The ranges of laser intensity for each beam line as it propagates from the focusing mirror to the target can readily be calculated. Intensity at the GIMM would be I_{mirror} ~1.3 GW/cm^2. The intensity of the focused laser beam at the target is on the order of 10^{14} W/cm^2. A plot of Prometheus laser intensity, $I_{laser}(z)$ as a function of distance, z, from the final turning mirror to beyond the target focal plane is shown in Figure 6.5.1-23.

Laboratory experiments have shown that laser-induced gas breakdown and plasma formation begins at intensities[14] at or above 10^{10} W/cm^2 (or 10 GW/cm^2). Thus, it is possible to consider placing a high-Z gas cell with pressures higher than a few millitorr at distances from the target greater than 8 m. The high Z gas cell (e.g., Pb or Xe [Xe might cause some gas-pumping problems]) could be used to protect the final optics from the softer x-rays. For neutron protection, a fill of Ne can be considered owing to the relatively large neutron cross-sections of low-Z atoms.

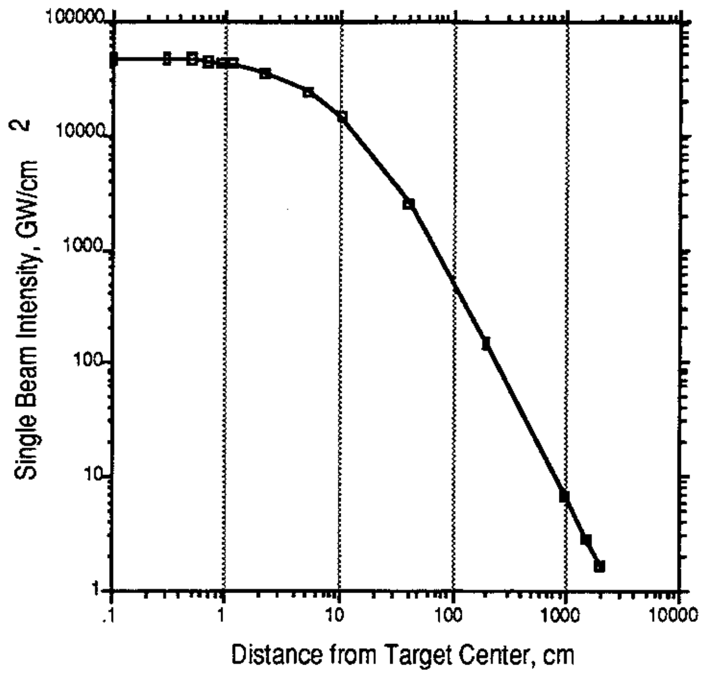

Figure 6.5.1-23 The single beam Prometheus laser intensity as a function of distance from a 6 mm diameter direct drive target with the beam diameter = target diameter at the target for a 100 kJ beam in a 6 ns pulse

Damage issues for the final focusing/turning optics arise from six sources:

(1) x-rays
(2) γ-rays
(3) neutrons
(4) laser radiation
(5) charged particles
(6) debris

Some of the properties of the five sources are summarized in Table 6.5.1-11.

Table 6.5.1-11
Potential Damage Sources for Final Turning Optics

Type of Source	Propagation Speed	Damage Threshold	Proposed Barrier
x-rays	$3x10^{10}$ cm/sec	0.5 MRad	Xe gas
γ-rays	$3x10^{10}$ cm/sec	0.5 MRad	Xe gas
neutrons	$5x10^{9}$ cm/sec	$4x10^{11}$/cm^2 (~1 J/cm^2)	Ne gas
laser light	$3x10^{10}$ cm/sec	8 J/cm^2	none
ions	1--$9x10^{9}$ cm/sec	0.1 J/cm^2	Ne/Xe gas
debris	0.2--$4x10^{7}$ cm/sec	0.5 J/cm^2	mech. shutter

The optical radiation emanating from the target chamber may move too rapidly for protection schemes to protect the GIMM. As discussed in the following section, since the laser beams enter the target chamber through restricting apertures located approximately 5 meters from the target, a time delay of ~16.7 ns will occur before this "prompt" radiation reaches the target chamber entrance apertures. The "prompt" radiation can ablate a plasma traveling at a speed of ~4×10^5 m/sec which may influence the passage of further optical radiation through the entrance apertures.

6.5.1.7.5 <u>Plasma Closure Inside Target Chamber</u> - Plasma closure of the laser beam entrance ports inside the target chamber were considered in order to evaluate this mechanism as potentially contributing to the protection of the final focusing optics from target radiation. The calculations are based upon the assumption that a complete DT target "burn" occurs; calculations of the expected behavior for "near misses" or "dud" targets (both with <u>no</u> thermonuclear output) may generate some non-charged, relatively large diameter (>1 μm) particles.

Previous work[14] carried out at the Lawrence Livermore National Laboratory on plasma closure of optical apertures revealed that laser induced plasmas reached critical densities (for illumination wavelengths of 1064 nm) at speeds of approximately 4×10^5 m/sec. The threshold for plasma formation was measured for intensities $>5\times10^{10}$ W/cm^2. Since the excimer lasers have significantly shorter wavelengths (λ_{KrF} = 248 nm and λ_{ArF} = 193 nm) than the wavelengths at which these measurements were made (λ_{Nd} = 1064 nm), a higher ion density will be required before the plasma critical density is reached for these shorter wavelengths. However, for plasmas generated by the impact of γ-rays, x-rays, and high energy neutrons with the wall material, a hotter (i. e., more energetic) plasma would be expected. Accordingly, it is estimated that the critically-dense portion of the plasma would arrive at a speed of 5×10^5 m/sec. There are four areas of interest:

(1) Plasma closure in the target chamber laser beam entrance ports
(2) Target debris ion speeds for Pb capsule hohlraum designs (for ID targets)
(3) Update of the configuration for SBS pulse compression in the target chamber vicinity
(4) Update of the Raman accumulator geometry for electric discharge excimer lasers.

Each of these areas is briefly described in the sections below.

<u>Plasma Closure from Ablation Products in Target Chamber</u> - The complete thermonuclear burn of the DT fuel capsule will generate roughly 500 to 1000 MJ of

energy primarily in the form of "prompt" radiation, i.e., particles and radiation moving at or near the speed of light, 3×10^8 m/sec. This "prompt" radiation consists of γ-rays, x-rays, and primarily 14 MeV neutrons. We assume further that the thermonuclear burn occurs over the time period of approximately 5 ns. As discussed in Section 3.0, ionized target debris derived from the explosion of the high-Z capsule moves at a significantly slower speed, $<4 \times 10^5$ m/sec. Thus, for a target chamber of radius R, the time delay, Δt, before the "prompt" radiation strikes the chamber wall is simply:

$$\Delta t = \frac{\;}{c} \qquad (6.5.1\text{-}9)$$

For $R = 5$ m, $\Delta t = 16.7$ ns. The X-ray portion of the "prompt" radiation is expected to ablate a plasma from the wetted wall of the chamber. This plasma expands outward from the wetted wall of the target chamber with an estimated speed of $v_p \sim 5 \times 10^5$ m/sec. A portion of this plasma will help stop the ionized debris from the exploded target capsule so that some of this debris may not reach the GIMM located at a distance $R_1 \sim 20$ m from the target.

The γ-rays and neutrons of the "prompt radiation" penetrate deeper into the first wall, and consequently a Pb vapor cloud will be ejected and expand into the target chamber. An expression for the rate of energy loss of an ionized particle of charge Q passing through a cloud of N neutral atoms/cm^3 is given by:

$$\frac{dE}{dr} = \frac{4\pi N Z Q^2 e^2}{m_e v_p^2}\left\{\ln\left[\frac{2m v_p^2}{\eta}\right] - \ln(1-\beta^2) - \beta^2\right\} \qquad (6.5.1\text{-}10)$$

where Z in the atomic number, v_p is the particle velocity, $\beta = v_p/c$ e is the electronic charge, m is the electron mass, and η is the ionization potential of the neutral atoms. The stopping distance, R_s, for the ionized particle can be calculated from:

$$R_s = \int_0^E \frac{dE}{-dE/dr} \approx \xi_p \frac{E_p}{Q^2 N} \qquad (6.5.1\text{-}11)$$

where E_p is the energy of the particle and $\xi_p(Z, E_p, N)$ is a constant. For charged particles passing through a plasma, dE/dr is even larger, resulting in increased Bremsstrahlung. For a few hundred millitorr of Pb vapor erupted from the first wall, preliminary calculations show Pb ions of up to 200 keV energy will be stopped in ~1 cm of vapor.

It should also be noted that the low-Z materials (e.g., C, H, D, & T) in the target should be included in these analyses since these elements may be numerically more abundant than the high-Z casing materials. Assuming that the low-Z elements have approximately the same kinetic energy spectrum as the high-Z (and assuming local thermodynamic equilibrium [LTE]), the velocities of the lightest isotopes will be approximately an order of magnitude greater than an element such as Pb. A schematic of this effect is illustrated in Figure 6.5.1-24.

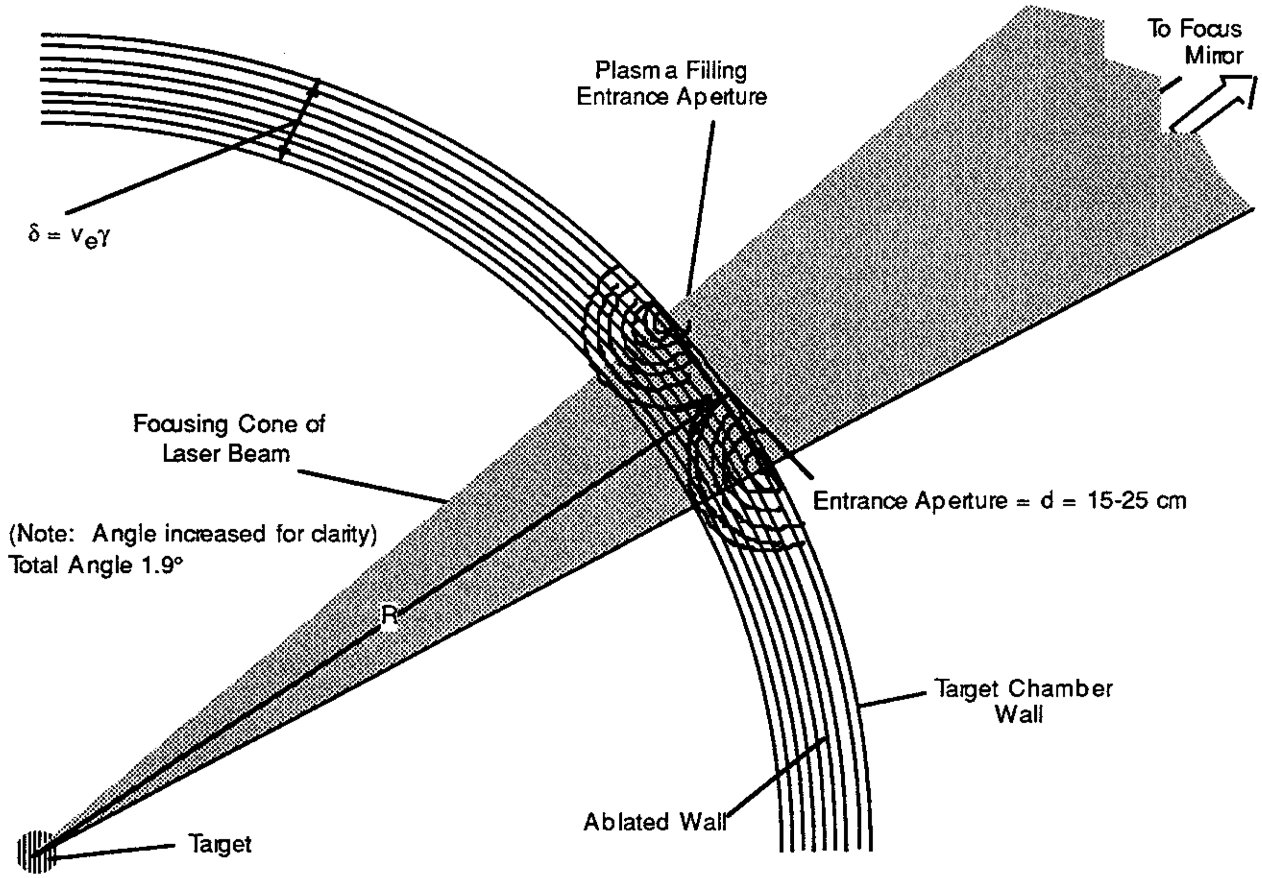

Figure 6.5.1-24 Schematic of Prompt Radiation for D/T Target Ablating Plasma from Reactor Chamber First Wall

As illustrated in Figure 6.5.1-24, the expanding plasma and vapors from the first wall around each of the optical beam entrance ports eventually will fill the beam ports. Although the fast-moving plasma may achieve "critical density" such that it is optically opaque, ions with energies > 100 keV have considerable penetration of the plasma. Assuming that the diameter of the optical beam entrance ports is d, then the length of time needed for the expanding plasma to fill these apertures is simply:

$$\tau = d/2v_p \qquad (6.5.1\text{-}12)$$

where v_p is the plasma expansion speed (v_p ~ 5x10^5 m/sec). A schematic of the arrangement of the ~1 m effective aperture final focusing mirror relative to the target chamber is shown in Figure 6.5.1-25.

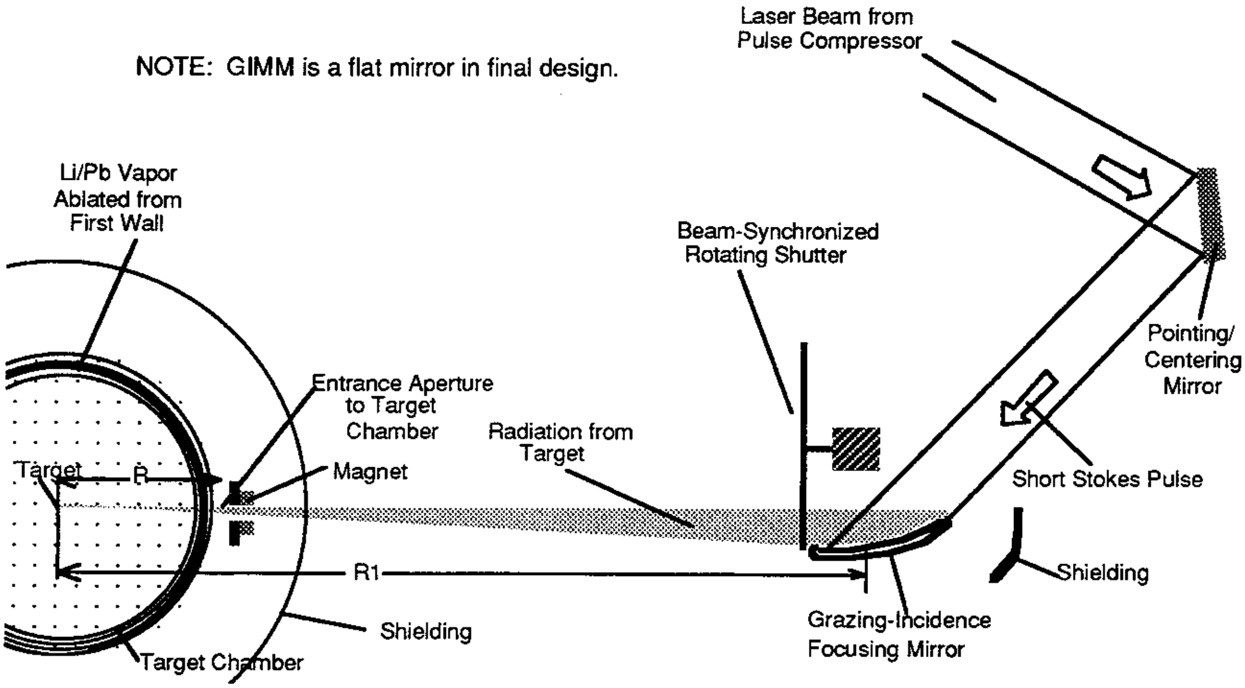

Figure 6.5.1-25 Schematic of Placement of Final Focusing Optics, Magnetic Deflector, Rotating Mechanical Shutter, and Input Laser Pulse Relative to Target Chamber

This geometry illustrates possible placements for an ion deflection magnet and a rotating "slow debris" mechanical shutter, both of which are intended to provide target debris protection for the final focusing mirror. As indicated in Figures 6.5.1-24 and 6.5.1-25, the approximate diameter, d, for the optical entrance port in the target chamber is estimated by

$$d = \xi D R / R_1 \qquad (6.5.1\text{-}13)$$

where D is the effective diameter of the focusing mirror, R_1 is the distance from the target to the grazing incidence focusing mirror, and ξ is an apodizing factor to guarantee that the near field laser beam intensity incident on the perimeter of the entrance port is below 10^{10} W/cm^2. For D =1 m, R_1 = 25 m, R = 5 m, and ξ = 1.2, d ~24 cm.

Calculations of Target Debris Velocity Spectra - Although the adopted target for the laser design is the direct-drive, the indirect-drive laser target was used as a more severe case to assess. Following a review of LLNL calculations of the target debris velocity spectra for different thickness indirect drive capsules, velocity spectra measured[15] by

Charles Orth were considered. In all cases, following the 500 to 1000 MJ burn, the high-Z capsule debris appears to be completely ionized (with many ions in the +3 ionization state) with essentially all heavy ions having energies less than 500 keV. For Pb ions, this energy is not relativistic, so the estimated speed spectra, v_p, of the particles follows the calculated energies (expressed in electron volts) from the expression:

$$v_p = \sqrt{\frac{2E_p e}{m}} \sim 7x10^5 m/s \qquad (6.5.1\text{-}14)$$

where E_p is the particle energy in electron volts, eis the electronic charge in coulombs, and m is the mass of the lead atom in g.

The indirect laser target is assumed to be subjected to two-sided illumination with two cones of approximately 50° each.

Although many of the details of the indirect drive laser target are not defined , the major features include the DT fuel capsule suspended within the high-Z case. Reductions in the required high-Z mass for the case may require more realistic designs for mass-produced targets for which the legacy of recovering large quantities of vaporized high-Z material would not be cost effective.

As mentioned earlier, not considered at this time is the problem of target debris generated when a target misfires, yielding little or no thermonuclear energy. Under these circumstances, non-charged, relatively small (~1 µm) particles could be expelled from the target chamber at relatively low speeds. A possible protection mechanism for this eventuality is illustrated in Figure 6.5.1-25 in which synchronized, high speed, rotating mechanical shutters close off each of the 60 final focusing optical system beamlines shortly after delivery of each laser pulse. With a shutter speed of 1 km/sec, a one-meter beamline could be protected in 1 ms.

By far the most common problem faced by the focusing optics is dealing with the fluence of γ-rays, x-rays, and high energy neutrons. Both the γ-rays and the neutrons will penetrate deeply into the final focusing mirror substrate, whereas the x-rays will be absorbed in the mirror surface (with the x-ray fluence reduced by cos θ). At present our plan is to design the final focusing mirror to survive the "prompt" radiation loading.

The slower debris from the target should be effectively attenuated by ablated plasma (and to a minor extent Pb vapor) from the first wall of the target chamber. Installation of a strong deflecting magnetic field near the target chamber will help keep charged particles away from the focusing optics.

Charged ion debris velocity spectra for the bare DT target is shown in Figures 6.5.1-26. The spectra for lead should also be included as it was selected for use in the case.

Thus the ions from the target should be effectively stopped in the residual Pb vapor present in the direct line of sight between the GIMM and the center of the target chamber.

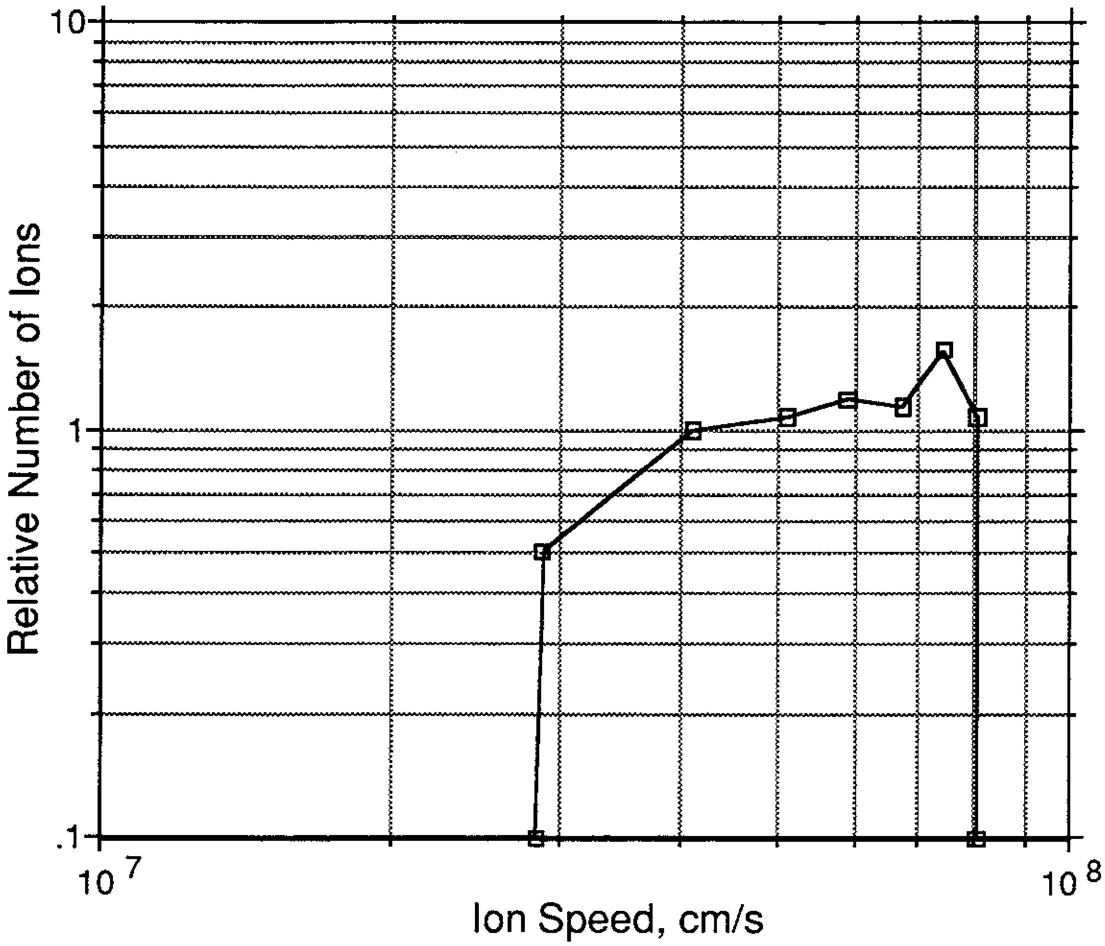

Figure 6.5.1-26 Target Debris Velocity Spectra for Bare D/T Target

6.5.1.8 Grazing Incidence Metal Mirror

In this section, the data base which is relevant to the material selection of the final Grazing Incidence Metal Mirror (GIMM) is presented. A unique design for the GIMM is then presented and analyzed.

6.5.1.8.1 **Introduction** - Transmission measurements for conventional dielectrics show that the absorption coefficient of MgF_2 and the optical transmission of ZnS for wavelengths of interest (250-500 mm) both degrade by an order of magnitude after 10^{16} n/cm^2. [16] This is an extremely low fluence limit, and even if most of the color centers are annealed out by periodic heating, residual defects would still remain and lead to an extremely short life time. For these reasons, a metal mirror surface is chosen as the final optical element in our laser system before focused laser light enters the cavity.

6.5.1.8.2 **Metal Reflectivity and Absorptivity for Laser Light** - The surface material for the GIMM must have the highest reflectivity and lowest absorptivity. This optimum choice is necessary so that the damage to the mirror's surface is minimized. Table 6.5.1-12 gives the room temperature for materials of interest. These values are experimental and are for polished surface reflectivity light of long wavelength (500-10,000 nm).[17]

Table 6.5.1-12. Reflectivity for Materials of Interest (Polished Surfaces)

Element	l (µm)	%R
C	0.5-10	22-59
Mg	0.5-9.0	72-93
Al	1-12	71-98
Si	0.5-10	34-28
Fe	0.5-9.0	55-92
Ag	0.8-9.0	96.8-98.7

In the wavelength of interest (i.e., 200 to 500 nm), metal reflectivities are strong functions of the wavelength (photon energy) and the angle of incidence. It is desirable to select a material which does not exhibit electronic absorption bands close to the operational regime of KrF laser. Figure 6.5.1-27 shows the reflectivity of Ag, Al, and Mg at normal incidence as a function of the wavelength. The strong photon-electron interaction in Ag for wavelength in the vicinity of 320 nm would exclude it from our list since the wavelength of KrF laser is 300 nm. At grazing incidence (q = 85°), the reflectivities of both Al and Mg markedly improve, as can be seen in Figure 6.5.1-28. For KrF laser light, the reflectivity of both Al and Mg is about the same (99.4%).

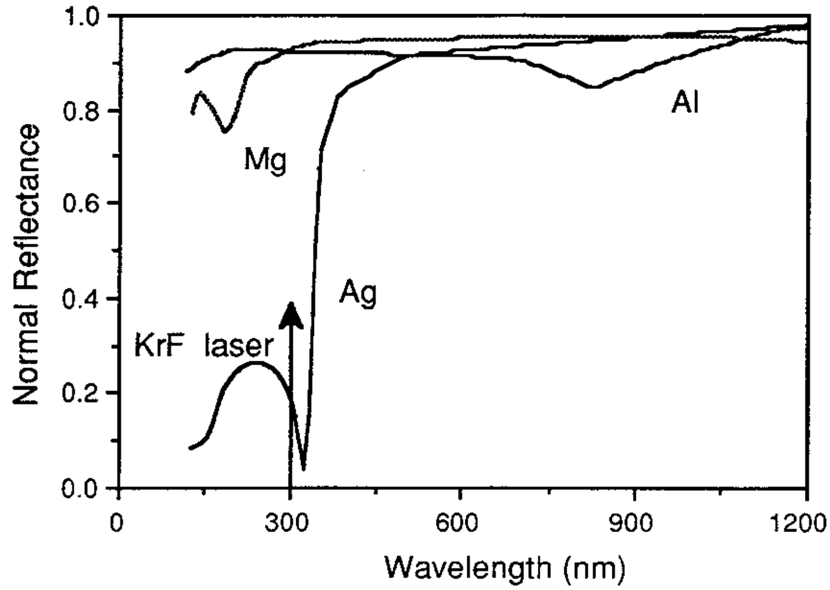

Figure 6.5.1-27 Reflectivities at Normal Incidence

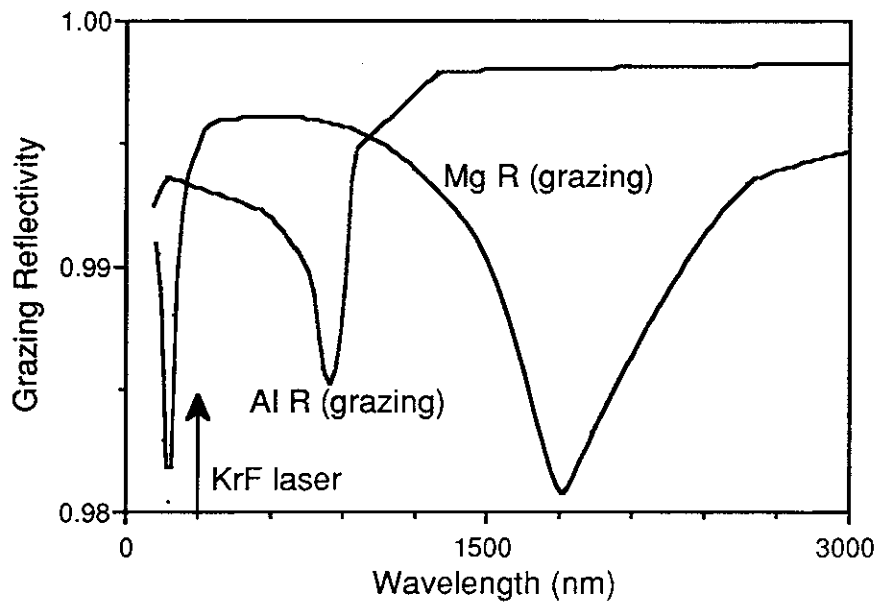

Figure 6.5.1-28. Reflectivities at Grazing Incidence (85°)

6.5.1.8.3 **Radiation Effects on Candidate Materials** - Neutron irradiation results in a number of detrimental effects to the mirror's optical performance. Defects, in the form of vacancies, interstitials, transmutations, and subsequent micro-structural changes, lead to deterioration of the focusing quality of the mirror and increase the absorption of incident laser light. The salient effects of neutron irradiation are discussed in the following sections, including how such effects can be accommodated. Main areas of concern are the effects of produced defects on increasing the electrical resistivity (and hence the laser light absorptivity) of the mirror and the deformation of the mirror's surface, leading to defocusing of the laser beam.

Radiation Effects on Resistivity and Surface Absorptivity - The increase in the resistivity of the aluminum layer will occur by the accumulation of point defects and transmutation products. The rate of increase in the resistivity due to point defects must saturate, either by overlap of neighboring collision cascades or by thermal annealing effects. The rate of resistivity change can be written as:

$$\frac{dP}{dt} = k\sigma_d\phi\rho_F - \frac{\rho}{\tau} \qquad (6.5.1\text{-}15)$$

where k is an efficiency factor, σ_d is the displacement cross-section, ϕ is the neutron flux, ρ_F is the measured resistivity increase per Frenkel Pair, and τ is the cascade lifetime in aluminum. The resistivity will saturate at a neutron fluence of $(\phi t)_{sat.} = \phi t$ (Eq. 6.5.1-15). At high temperatures, t is very short and resistivity saturation will occur at a very small fluence (on the order of $x10^{17}$-10^{18} n/cm^2).

At cryogenic temperatures (77 K), the corresponding change in the mirror's absorptivity is reported to be less that 1% at normal incidence and less than 0.5% at grazing incidence.[2] In our design, however, the aluminum surface will run hot, and point defect annealing will result in a further decrease in the magnitude of the irradiation-induced absorptivity.

The contribution of transmutations to the increase in resistivity and, hence, the absorptivity of the surface does not saturate, as is the case with point defects. However, the resistivity increase per transmutation atom is 4-5 orders of magnitude less than that for point defects.[2] For this reason, their contribution during the mirror's lifetime will be negligible.

Sputtering of surface atoms can lead to roughening. It is experimentally estimated that the sputtering yield of 14 MeV neutrons is on the order of $5x10^{-4}$ per neutron.[18] If a gas shield is introduced to protect from x-rays, additional sputtering from argon atoms will contribute by a small amount,[17] on the order of 6% of the neutron sputtering value.

These sputtering events can lead to surface features which would destroy the quality of the laser beam. Since the aluminum surface temperature will be high, rapid atomic surface diffusion is expected to result in the removal of layer-by-layer from the surface of the mirror.

In conclusion, it is estimated that the total increase in absorptivity of the mirror due to point defects, transmutations, and sputtering is on the order of 0.5% and that it will saturate after few days of operation. For all practical purposes, therefore, the reflectivity for 300 nm laser light will degrade to 99%; i.e., only 1% of the light will be absorbed.

Neutron-Induced Swelling - When non-uniform swelling takes place in the aluminum layer, gradients in surface displacements will occur. Focusing of the laser light may become impossible if surface undulations on the order of 1/4 of the wavelength result. This tolerance (about 75 nm) is very strict and has actually resulted in very short lifetimes for similar mirrors in other conceptual designs.

Neutron swelling data on aluminum and magnesium show strong dependence on the impurity level. Experimental data of Adda[18] are summarized in Figures 6.5.1-29 and 6.5.1-30. The base case for our design (99.994% purity) is replotted in Figure 6.5.1-31, where the swelling is shown as a function of the high energy neutron fluence. It is clear from this figure that aluminum will be a better choice for the mirror's surface than magnesium. The following design equation is used to fit the swelling data of aluminum and magnesium:

$$\frac{\Delta V}{V}\% = k\phi t \qquad (6.5.1\text{-}16)$$

where k is a constant, and $\phi\tau$ is the neutron fluence in n/cm^2. For Mg, $\kappa = 1.29 \times 10^{-21}$ and, for Al, $\kappa = 1.11 \times 10^{-21}$.

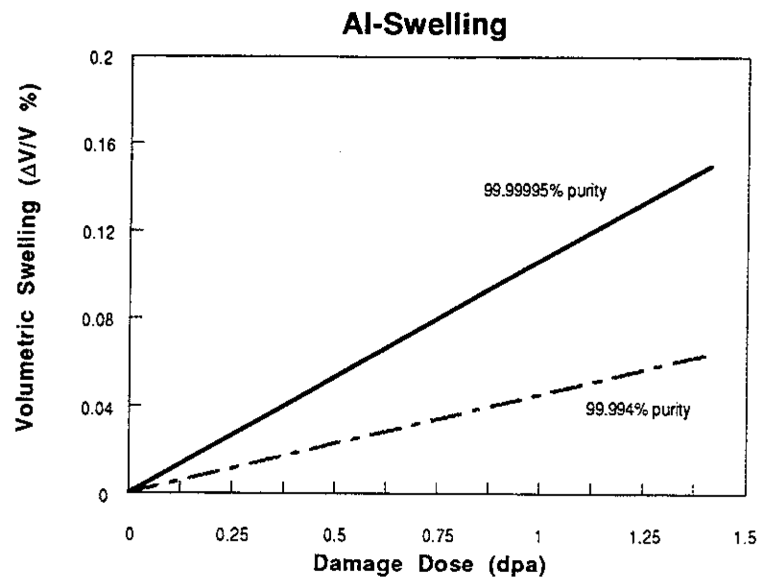

Figure 6.5.1-29 Neutron-Induced Swelling in Aluminum[18]

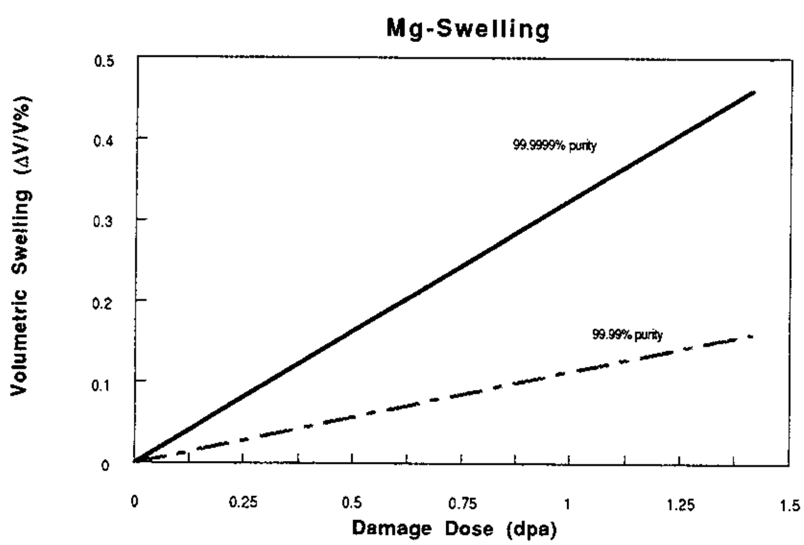

Figure 6.5.1-30 Neutron-Induced Swelling in Magnesium[18]

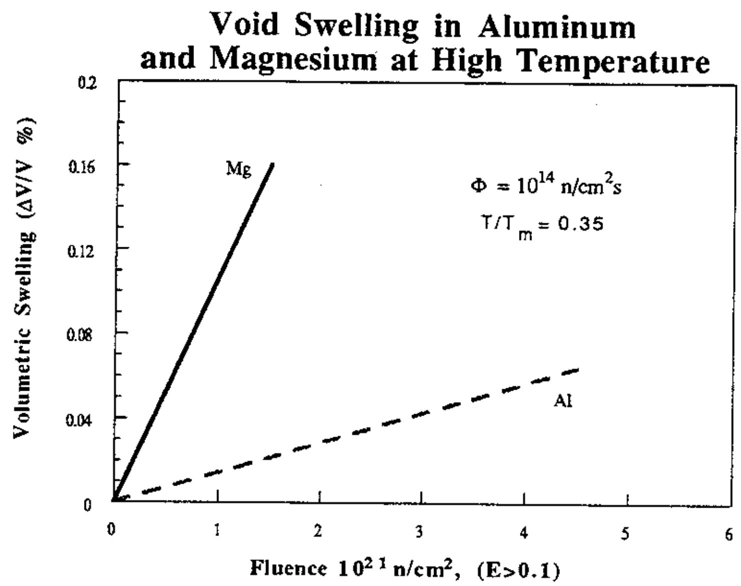

Figure 6.5.1-31 Void Swelling at High Temperature

6.5.1.8.4 Configuration and Material Selection - The basic design philosophy of the mirror is to separate the functions of each material. For this reason, a high reflectivity aluminum surface is created by a CVD process on top of a SiC structure. The SiC structure is stiffened in two transverse directions by two sets of I-beams. The surface is cooled by flowing helium through the coolant channels. A top view of the mirror is shown in Figure 6.5.1-32. Mirror sizing is dictated by two factors:

(a) Maximum temperature rise in the aluminum during the laser pulse should not exceed the re-crystallization temperature.

(b) Induced thermal stress in the aluminum layer should not exceed its fatigue endurance limit.

Design Rationale For The GIMM - The optical properties of the mirror's surface have been decoupled from the mechanical properties of the supporting structure. In this regard, we have achieved a great degree of flexibility in the design. The surface of the GIMM is metallic because dielectric materials show great sensitivity to the effects of ionizing radiation.

The leading high reflectivity candidate metals are aluminum, magnesium, silver, gold, and copper. The following criteria were used to select between these metals:

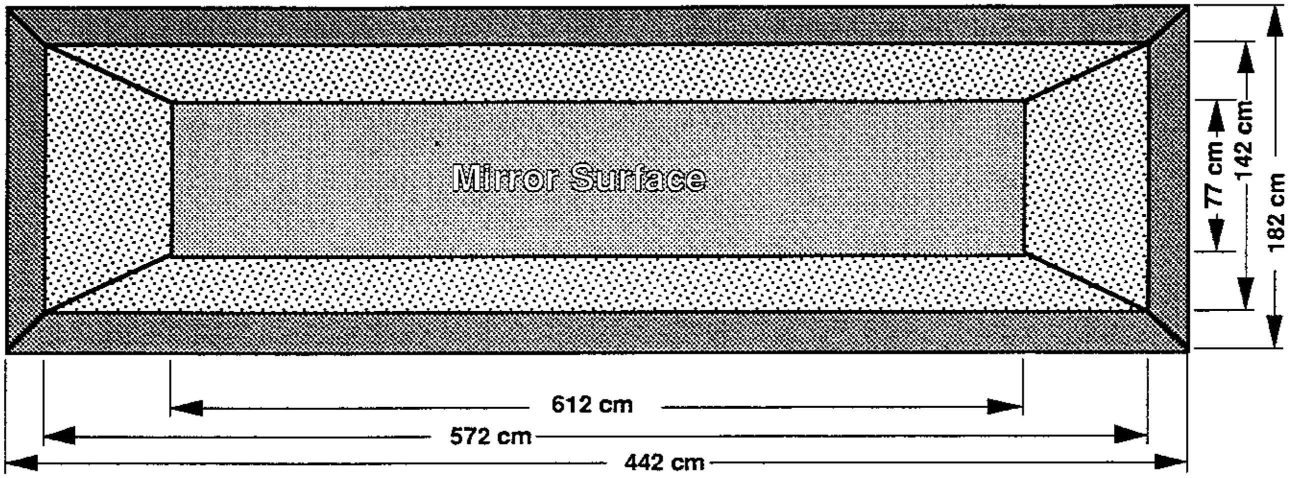

Figure 6.5.1-32. Top View of GIMM with Scaled Measurements.

(1) High reflectivity in the wavelength of interest (i.e., 250 to 500 nm)
(2) Effects of radiation on absorptivity
(3) Surface temperature rise during the laser pulse
(4) Thermal fatigue resistance
(5) Radiation effects on surface deformation

Although silver has excellent reflectivity, neutron-induced micro-craters are expected to distort the mirror's surface. Near-surface collision cascades in silver are very dense because of the high electronic stopping power of silver. Copper was excluded on the basis of its high neutron-induced swelling, particularly when it is pure. The higher fatigue strength of aluminum results in a smaller mirror size when it is compared to magnesium. In addition, the neutron-induced swelling rate of commercial grade aluminum is lower than that of magnesium. For the above reasons, aluminum is selected as the material for the reflective surface of the mirror.

Structural support of the mirror is composed of two parts: a low swelling composite SiC high-rigidity support structure and a concrete support frame for control of thermal deformations. The SiC structure is composed of small helium cooling channels, running along the length of the mirror. Two other layers are attached immediately underneath. Each one of these two layers is stiffened by I-beams. A SiC composite structure was chosen for the following reasons:

(1) Very low neutron-induced deformations by thermal and irradiation creep mechanisms in the temperature range of 500 to 700 K.
(2) For porosity of approximately 10-15%, no neutron swelling is to be expected; thus, mechanical deformations of the mirror's surface are minimized.
(3) SiC is a low activation material. The choice of SiC will allow passive safety and shallow land burial of the mirror at the end of life.

The SiC structure is surrounded by a concrete frame to provide complete to restrict out-of-plane deformations. A sliding bolt mechanism between the SiC strucure and the concrete frame compensates for all movement.

Since the coefficient of thermal expansion of aluminum is higher than that of SiC, a shear graphitic layer is deposited first on the surface of the SiC composite, and the aluminum is added on top of the graphitic shear layer . With this arrangement, in-plane mismatch thermal expansions of the aluminum can be isolated from the SiC composite structure.

A GIMM cross-section is shown in Figure 6.5.1-33 and the details are illustrated in Figure 6.5.1-34. Thermal expansion gaps are provided around the mirror structure to prevent buckling. The main structure of the mirror (SiC) is surrounded by a rigid concrete frame structure. This mirror support structure is designed to prevent mirror deflections by distributed clamping forces, over a 30 cm distance, as shown in Figure 6.5.1-35. The magnitude of the distributed clamping forces will be calculated in the section on surface deformations.

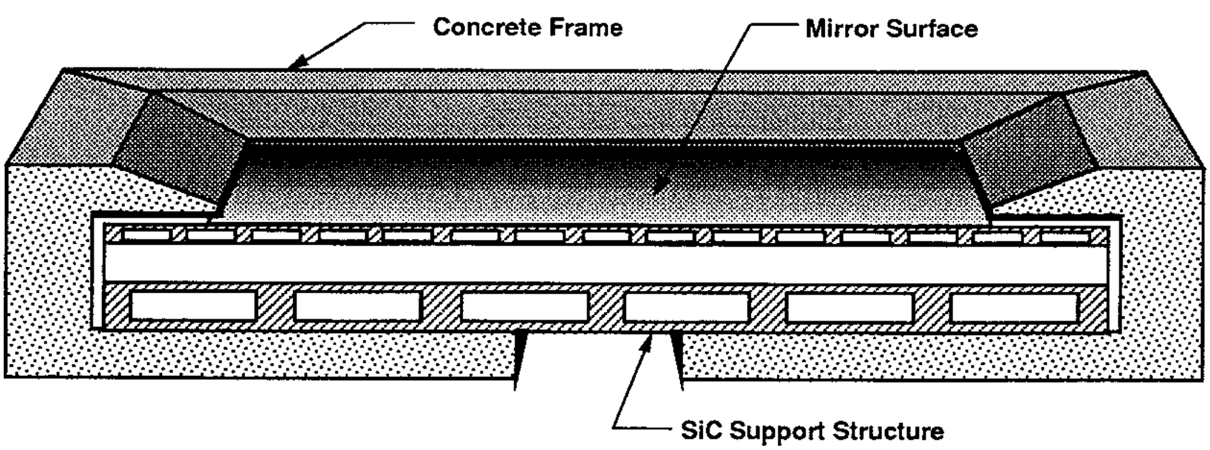

Figure 6.5.1-33. Cross-Sectional View of GIMM

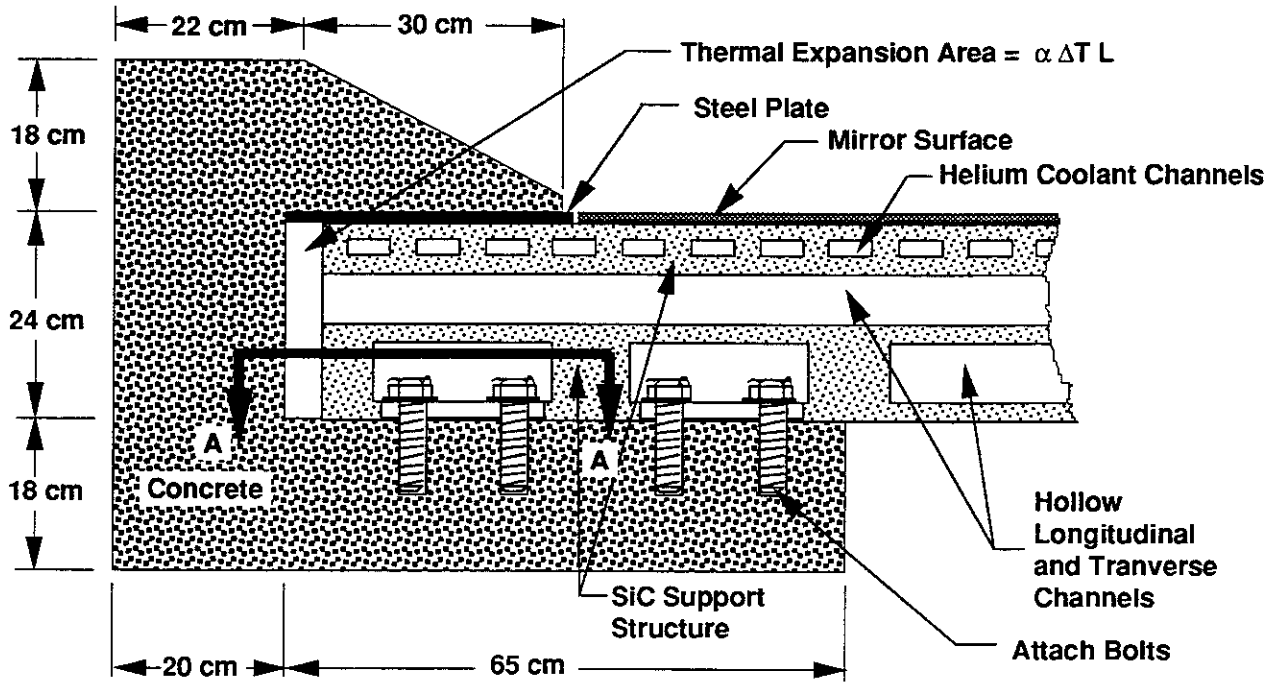

Figure 6.5.1-34. Detailed Cross-Section of GIMM

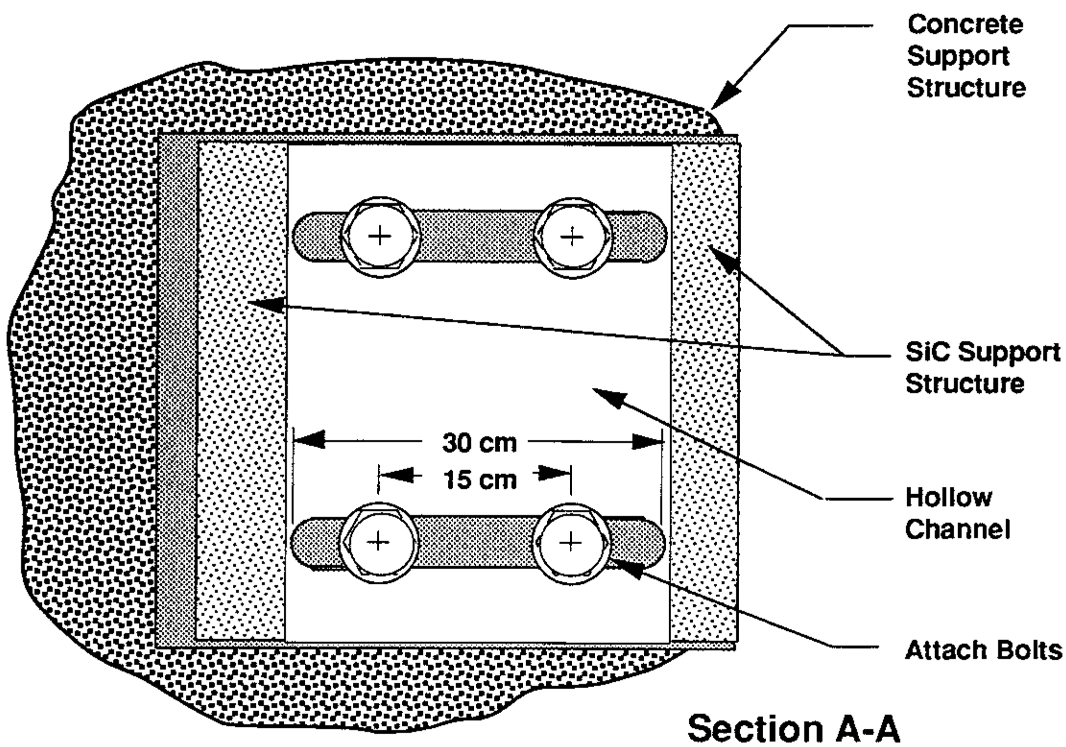

Figure 6.5.1-35. Section View of Mirror Structure Illustrating Expansion Capability

6.5.1.8.5 GIMM Thermal Design - Steady-state temperature gradients and the instantaneous rise in the mirror's surface temperature are minimized by cooling. Cooling concepts existe to control the steady-state temperature gradients, but the instantaneous surface temperature rise is almost a material property, since the duration of the laser pulse (a few ns) is much shorter than typical thermal diffusion times. The optical penetration distance of the laser light is given by:

$$d = \frac{\lambda}{4\pi k} \qquad (6.5.1\text{-}17)$$

where λ is the wave length, and k is the extinction coefficient. A KrF laser penetrates aluminum only 7 nm for normal incidence, and about 2-3 atomic layers for grazing incidence. Therefore, a good approximation to the surface temperature will be an instantaneous temperature rise given by:

$$\Delta T_s = \frac{2(1-R)q_{beam}}{k}\sqrt{\frac{\alpha t}{\pi}} \qquad (6.5.1\text{-}18)$$

where q_{beam} is the instantaneous surface power density and t is the duration of the laser pulse. k, α, and R are for the aluminum surface.

The mirror is designed with convective helium cooling channels as shown in Figures 6.5.1-32 and 6.5.1-33. Since heat loss from the bottom surface of the mirror is very small, the temperature gradient through the mirror will be slightly greater than across the cooling channel thickness. Temperature and convective heat transfer calculations across the cooling channel are shown in Table 6.5.1-13.

Table 6.5.1-13. Thermal-Hydraulic Parameters for the GIMM

Parameter	Value	Units
Wall Temperature	450	K
Bulk Temperature	350	K
Pressure Exit	1	MPa
Pressure Drop	19.58	Pa/m
Bulk Velocity	20	m/s
Reynolds Number	2.47×10^5	
Heat Transfer Coefficient	261	W/mK

The temperature drop across a 2-cm channel wall at the average heat flux can be computed as follows:

Total mirror surface area = number of mirrors x width x length = 60 x 77 x 442
$= 2.04 \times 10^6\ cm^2$

Energy Density per pulse $= \dfrac{5\,MJ}{2.04 \times 10^6} = 2.45\ J/cm^2$

Absorbed energy density per pulse = 0.01 x 2.45 = 0.0245 J/cm^2

Average heat flux = 3.5 x 0.0245 = 0.08575 W/cm^2.

If the conductivity of SiC is taken as 0.20 W/cm/K (for irradiated SiC at low temperature), then the temperature drop across the support structure will be on the order of 2 K. The effective coolant channel thickness is taken as 4 cm. This small temperature drop must be taken into account for calculations of the thermal deflections of the mirror's surface.

When the laser energy is delivered in a short pulse (7.3 ns), the instantaneous power is very high. The rise in the surface temperature of the mirror is mainly dictated by the thermal diffusivity of the aluminum. Calculations with Eq. 6.5.1-18 above give the results shown in Table 6.5.1-14. The instantaneous surface temperature rise is 130.6 K. The corresponding thermal stress can simply be found as:

$$\sigma \approx \frac{E}{(1-\nu)} \alpha \Delta T \qquad (6.5.1\text{-}19)$$

Using the properties of aluminum (annealed material), the following is obtained:

$$\sigma = \frac{63.8 \times 10^3}{(1-0.34)} \times 25 \times 10^{-6} = 130.6\,MPa \qquad (6.5.1\text{-}20)$$

This may exceed the fatigue endurance limit of some aluminum alloys. (It is in the range of 50-390 MPa.) However, if the radiation hardening effects are considered, the endurance limit can be raised by as much as 50 MPa for aluminum.[19]

6.5.1.8.6 GIMM Mechanical Deformation - Out-of-plane deformation of the mirror's surface should be minimized, or eliminated, if high quality laser beams are to be maintained. Two primary sources of deformation must be analyzed.

(1) Thermal deformation
(2) Neutron-induced swelling deformation

The design approach is to isolate these two effects. In this respect, an aluminum metal surface and an SiC backing is used. The temperature of SiC can be kept low enough

Table 6.5.1-14. Thermo-Physical Properties of High Purity Aluminum

Parameter	Symbol	Value	Units
Thermal Conductivity	k	2.4	W/cm K
Density	ρ	2.7	g/cm^3
Specific Heat	c_p	0.95	J/gm K
Thermal Diffusivity	γ	0.936	cm^2/s
Characteristic Thermal Diffusion Distance	<d>	0.466	μm
Average Energy Density	<E>	2.45	J/cm^2
Average Power Density During Pulse	<q>	3.36E+08	W/cm^2
Average Absorbed Power Density	$<q>_0$	3.36E+05	W/cm^2
Temperature Rise During Pulse	ΔT	130.6	K

that neutron-induced swelling is eliminated. Therefore, the design must eliminate the deformation of the SiC plate as a result of the modest temperature gradient of a few degrees. When this is accomplished, the deformation of the aluminum surface by neutron swelling should be compensated for separately.

The theory of plates and shellsis an appropriate theory for calculating the surface deformations. However, a good approximation is the elementary beam theory applied in the two transverse directions. The influence of in-plane shear is neglected in this case.

Consider the elementary theory of straight beams, as illustrated in Figure 6.5.1-36. The axial strain, ε_z, is given by:

$$\varepsilon_z = \frac{x}{\rho} \qquad (6.5.1\text{-}21)$$

where x is the distance off the neutral axis, and ρ is the radius of curvature of the mirror's surface. We know, however, that the mirror's curvature is given by:

$$\frac{1}{\rho} = \frac{d^2 v}{dz^2} \qquad (6.5.1\text{-}22)$$

where υ is the deflection of the mirror's surface, which we try to minimize, or better yet, eliminate.

Combining Eqs. 6.5.1-21 and 6.5.1-22, we obtain a relationship between the strain, ε_z, and the deflection of the mirror's surface. This is of the form:

$$\varepsilon_z = x\frac{d^2v}{dz^2} \qquad (6.5.1\text{-}23)$$

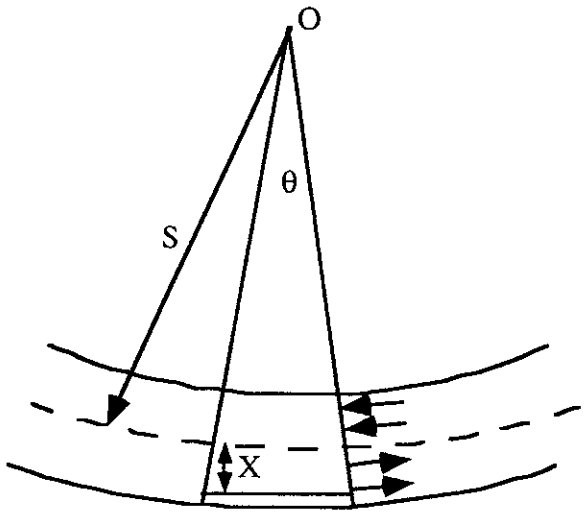

Figure 6.5.1-36. Thermal Design of the GIMM

The total axial strain at any distance, x, off the neutral axis is composed of an elastic component, σ/E, and two other inelastic components, αT and ε^s. αT is the thermal strain, while ε^s is the swelling strain. Now Eq. 6.5.1-23 can be put in the form:

$$x\frac{d^2v}{dz^2} = \frac{\sigma}{E} + \alpha T + \varepsilon^s \qquad (6.5.1\text{-}24)$$

The composite SiC structure is designed to exhibit very low swelling at high temperature by control of its internal porosity. At low temperature, as is the case in the GIMM, neutron irradiation will produce no swelling. The damaging neutron fluence is estimated from the uncollided neutron flux as:

$$\phi_u \approx \frac{S_0}{4\pi R^2} \qquad (6.5.1\text{-}25)$$

where the neutron slowing down and multiple scattering effects are neglected. For example, at the center of the mirror,

$$\phi_u \approx 1.957\text{x}10^3\ \text{n/cm}^2\text{/s} \qquad (6.5.1\text{-}26)$$

with a displacement cross-section of 3140 barns, the flux translates to a defect production rate of:

$$p = \phi_u \sigma_d \approx 2\,\text{dpa/yr} \qquad (6.5.1\text{-}27)$$

Detailed neutronics calculations are costly and are probably not warranted at this stage. Such calculations will lead to more accurate results than those given by

Eq. 6.5.1-27. However, it is clear that the swelling of SiC will be zero under these conditions and can, therefore, be eliminated from Eq. 6.5.1-24.

Multiplying both sides of Eq. 6.5.1-24 by bx, where b is the mirror's width, and integrating between -h and +h, where h is the mirror's height, the following is obtained:

$$\frac{d^2v}{dz^2} b \int_{-h}^{h} x^2 dx = \frac{1}{E} b \int_{-h}^{h} x\sigma dx + \alpha b \int_{-h}^{h} Txdx \qquad (6.5.1\text{-}28)$$

Assuming a linear temperature variation across the thickness of the mirror yields:

$$T = \frac{\Delta T}{2L} X \qquad (6.5.1\text{-}29)$$

where ΔT is the temperature difference between the top and bottom surfaces of the mirror. Inserting Eq. 6.5.1-29 into Eq. 6.5.1-28 and performing the integrations, the mirror's deflection equation is obtained:

$$\frac{d^2v}{dz^2} = \frac{M}{EI} + \frac{\alpha \Delta T}{2h} \qquad (6.5.1\text{-}30)$$

where M is the acting moment at any specific point in the mirror. The mirror is designed such that v=0 everywhere on the mirror's surface. This can be achieved via Eq. 6.5.1-30 by requiring that:

$$\frac{d^2v}{dz^2} = 0 \qquad (6.5.1\text{-}31)$$

and clamped end condition (i.e., $v(0) = v'(0) = v(l) = v'(l) = 0$). The solution to Eq. 6.5.1-30 will yield identically zero deflection everywhere.

This situation can be realized in one of two ways:

(1) Apply a uniform moment by force couples at distributed locations on the mirror's bottom surface.
(2) Clamp the edges of the mirror to produce a uniform moment everywhere on the mirror's surface. The clamping moment is given by:

$$M = -EI \frac{\alpha \Delta T}{2h} \qquad (6.5.1\text{-}32)$$

The second design approach is adopted. Clamping forces may be applied either as concentrated force couples, or distributed over a clamping distance, 2L. The required clamping force per unit length along the clamp, P, is numerically equal to M/L^2.

Using the properties of SiC and a temperature drop of 2.0°C (as was shown in the previous section), the clamping force per unit length is given by:

$$P = \frac{M}{L^2} = \pm EI \frac{\alpha \Delta T}{2hL} \qquad (6.5.1\text{-}33)$$

6.5.1.8.7 Neutron-Induced Mirror Surface Swelling - Using only non-collided neutron flux as a first approximation, the displacement rate at any point on the mirror's surface, a distance R away from the cavity center is given by:

$$R = (\phi t)\sigma\,(dpa\,/\,fpy) \qquad (6.5.1\text{-}34)$$

It is interesting to note from the above analysis that the surface deformation will be a function of the thickness of the aluminum layer. Figure 6.5.1-37 shows the various locations along the mirror's surface. The deformation is analyzed in the following two cases:

(1) Uniform aluminum layer thickness of 1 mm.
(2) A linearly graded thickness of 2 mm at the leading edge of the mirror, down to 1 mm at the trailing edge.

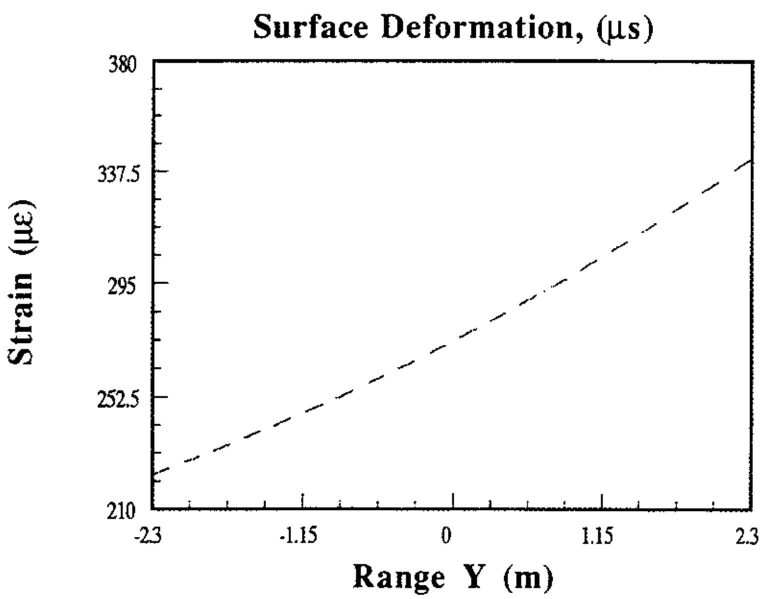

Figure 6.5.1-37. Surface Deformation of Mirror

In the first case, the difference in the normal deformation between the leading and trailing edges is

$\Delta \approx 112$ nm

which suggests that the lifetime of the mirror will be about one full power year. On the other hand, if the mirror's surface is linearly graded, this difference is given by:

$\Delta = 332.2 \times 1.0 - 223 \times 1.5 = 2.3$ nm

It is concluded, therefore, that the GIMM may last for plant lifetime if the present design is adopted.

References for 6.5.1

1. J. M. Auerbach, N. C. Holms, J. T. Hunt, and G. J. Linford, "Closure Phenomena in Pinholes Irradiated by Nd:Laser Pulses," Applied Optics, 18, 510 (1979).

2. TRW IOC from Gary Linford to Les Waganer, "Prometheus Telephone Contact Report: John Lindl/LLNL," K323-L-91-79, 10 May 1991.

3. Charles D. Orth, "Improved Understanding of First-Wall Vaporization-Condensation in Inertial Confinement Fusion Reactors," Fusion Technology, 10, pp. 1245--1250, (1986).

4. TRW IOC from Gary Linford to Les Waganer, "Initial Response to Comments by David Harris: LANL," K323-L-91-80, 12 May 1991.

5. John A. Hanlon and John McLeod, "The Aurora Laser Optical System," Fusion Technology 11, pp. 636-653 (1987).

6. Louis A. Rosocha, et al., "Aurora Multi-kJ KrF Laser System Prototype for Inertial Confinement Fusion," Fusion Technology 11, pp. 497-531 (1987).

7. Louis A. Rosocha and Kenneth B. Riepe, "Electron-Beam Sources for Pumping Large Aperture KrF Lasers," Fusion Technology 11, pp. 576-611 (1987).

8. J. E. Jones, et al., "Performance of the Aurora KrF ICF Laser System," Proceedings of the International Conference on Lasers '89, pp. 88-95, 3-8 December 1989.

9. Shirley J. Pfeifer, K. Allardyce, R. Johnson, G. Linford, H. Injeyan, and J. Betts (TRW Applied Technology Division, Redondo Beach, CA) and H. Komine, G. Lombardi, W. Long, and E. Stappaerts (Northrop Research & Technology Center) "Raman Beam Combining Program," Final Report for Contract #F29601-85-C-0053, prepared for the Air Force Weapons Laboratory, Kirtland Air Force Base, NM, September 1986.

10. Jerry Oldenettel and Michael Terpka, "Raman Oscillator Studies," Final Report for Contract F29601-84-C-0051, prepared for AFCMD, Kirtland AFB, NM, by Western Research Corporation, San Diego, CA, March 1987.

11. Mark Kushner, et al., "New Techniques for KrF Laser Fusion Systems," Interim Report for Los Alamos National Laboratory by Spectra Technology, Inc., Seattle, WA, 1989.

12. Arthur A. Mak and Leonid N. Soms, "Optical Methods for Laser Beam Control," Proceedings of SPIE, Vol. 1415, Modeling and Simulation of Laser Systems II, pp. 110-119, (1991).

13. W. Kaiser, M. Maier, "Stimulated Rayleigh, Brillouin, and Raman Spectroscopy," Laser Handbook, edited by F. T. Arecchi, North-Holland Book Co., pp. 1116-1120.

14. J. M. Auerbach, N. C. Holms, J. T. Hunt, and G. J. Linford, "Closure Phenomena in Pinholes Irradiated by Nd:Laser Pulses," Applied Optics, 18, 510 (1979).

15. Charles D. Oreth, "Improved Understanding of First-Wall Vaporization-Condensation in Inertial Confinement Fusion Reactors," Fusion Technology, 10, 1245 (1986).

16. M. J. Weber, Handbook of Laser Science and Technology, Vol. III, Optical Materials; Part 1, pages 336 and 366, CRC Press. Inc., 1986.

17. Robert Bieri and Michael Guinan, "An Analysis of Grazing Incidence Metal Mirrors in a Laser ICF Reactor Cavity," Lawrence Livermore Report, September 1990.

18. Y. Adda, "Report on the CEA Program of Investigations of Radiation-Induced Cavities in Metals," Proc. of the 1971 International Conference held at Albany, NY, June 1971.

19. D. S. Billington and J. S. Crawford, Jr., "Radiation Damage in Solids," Princeton University Press, Princeton, NJ (1961)